CHALMERS
UNIVERSITY OF TECHNOLOGY

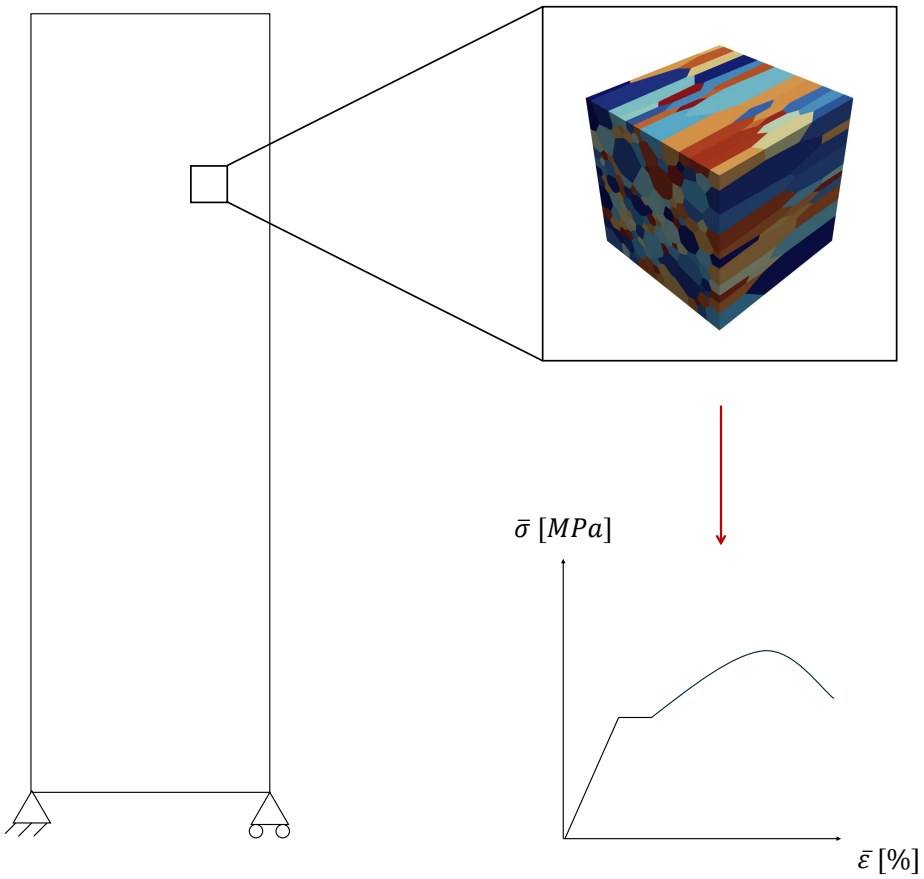

Evaluation of numerical prediction tools for anisotropic elasticity and plasticity in additively manufactured superalloys

Master's thesis in Structural Engineering and Building Technology

RAUAN AL-EMRANI

Department of Industrial and Materials Science
CHALMERS UNIVERSITY OF TECHNOLOGY
Gothenburg, Sweden 2024

Master's thesis IMSX30

Evaluation of numerical prediction tools for anisotropic elasticity and plasticity in additvely manufactured superalloys

RAUAN AL-EMRANI

CHALMERS
UNIVERSITY OF TECHNOLOGY

Department of Industrial and Materials Science
Chalmers University of Technology
Gothenburg, Sweden 2024

Evaluation of numerical prediction tools for anisotropic elasticity and plasticity in additvely manufactured superalloys

Supervisors:
Jim Brouzoulis, Chalmers University of Technology
Magnus Ekh, Chalmers University of Technology
Examiner: Magnus Ekh, Chalmers University of Technology

Chalmers University of Technology
SE-412 96 Gothenburg
Telephone +46 31 772 1000

Cover: A macroscale beam where a part of the microstructure is represented by an RVE with elongated grains which exhibits a certain homogenized stress-strain response.

Typeset in LaTeX
Printed by Chalmers Reproservice
Department of Industrial and Material Science
Gothenburg, Sweden 2024

Evaluation of numerical prediction tools for anisotropic elasticity and plasticity in additvely manufactured superalloys
Master's thesis in Structural Engineering and Building Technology
RAUAN AL-EMRANI
Department of Industrial and Material Science
Chalmers University of Technology

Abstract

During recent years, there has been an increasing interest in additively manufactured superalloys for load carrying structures. However, to fully utilize these components, it is necessary to understand how the material response depends on the microstructure. For this purpose, multiscale modelling is often used with crystal plasticity and FEM (CPFEM) for metals. While this method gives accurate results, it is computationally demanding. However, recent research at Chalmers has resulted in a new method, J-AMEN, which does not require FEM analysis and is less time consuming.

This thesis aims to compare CPFEM and J-AMEN, in order to investigate if J-AMEN gives as accurate results as CPFEM, while requiring significantly less computational time. This will be done for isotropic grain structure with equiaxed grains and an anisotropic grain structure, elongated grains, which are represented by Representative Volume Elements (RVE's). Two alloys will be investigated: Alloy 718 and Alloy720Li. The response during loading will be studied using virtual testing of the RVE's to compute both the homogenized stress-strain response as well as the individual grains' stress-strain behavior. Both elasticity and plasticity will be studied. Additionally, in the plastic analysis, the texture development of the grains will be studied.

For the elastic analyses, there is no significant difference in computational time when comparing the two different methods. Therefore, either of the homogenization methods could be used for multiscale modeling in elasticity and still produce accurate results. However, in the plastic analysis it can take up to several hours to do the CPFEM analysis, while J-AMEN gives results almost instantly. When comparing the homogenized stress-strain behavior for plasticity, J-AMEN gives an almost identical material response to that from CPFEM. Therefore, J-AMEN can be replaced with CPFEM for this type of analysis. The texture analyses for the different grain morphologies and the plasticity analysis for elongated grains was only conducted for CPFEM, as it was not possible to further expand J-AMEN during the time frame of this thesis. By developing J-AMEN in the future, these additional analyses could be included, and the results can then be compared with the CPFEM results in this report.

Keywords: Additive manufacturing, Crystal plasticity, Finite Element Method, Microstructure, Elasticity, Plasticity, Equiaxed grains, Columnar grains, Material modeling, Multiscale modeling.

Acknowledgements

This Master's thesis was written during the 2024 spring semester as a part of the *Structural Engineering and Building Technology* master's program at Chalmers University of Technology. The project was conducted at the division of *Material and Computational Mechanics*, at the department of *Industrial and Materials Science*.

The finite element computations in ABAQUS were enabled by resources provided by Chalmers e-Commons at Chalmers (C3SE).

First and foremost, I want to begin by thanking my supervisors Magnus Ekh and Jim Brouzoulis for their support and guidance throughout these past months. Because of you, working on this thesis has been incredibly fun. You have not only provided me with help and knowledge, but through your work you have showed me how to research, which is something that I will take with me in my future work. Additionally, I want to thank Björn Andersson for teaching me how to use the cluster and for always being available and eager to help me when I needed it.

I also want to thank my friends Elsa and Alice, for being my loyal lunch buddies during this master's thesis time. Lastly, I want to thank my opponents and friends Saffa and Cecilia for providing me with great feedback on my thesis and for making these last years at Chalmers so enjoyable.

Rauan Al-Emrani, Gothenburg, June 2024

Acronyms

AM - Additive manufacturing

CPFEM - Crystal plasticity finite element method

CRSS - Critical resolved shear stress

EPSC - Elastic-plastic self-consistent

FCC - Face-Centred Cubic

FEM - Finite element method

J-AMEN - Julia-Analysis and Modelling Service for Engineering Materials Studied with Neutrons

PBF - Powder bed fusion

rcl - Relative characteristic length

RVE - Representative volume element

Notations

γ - Accumulated plastic shear strain

$\dot{\gamma}^{\alpha}$ - Plastic slip rate on system α

$\dot{\boldsymbol{\varepsilon}}^{p}$ - Plastic shear rate

σ - Tensile stress

τ^{α} - Resolved shear stress

τ_0 - Critical resolved shear stress

$\mathbb{C}$ - Elastic stiffness tensor of a single crystal

$\mathbf{E}^{e}$ - Elastic strain tensor

$\mathbf{F}$ - Deformation gradient

$\mathbf{F}^{e}$ - Elastic component of deformation gradient

$\mathbf{F}^{p}$ - Plastic component of deformation gradient

g^{α} - Critical shear stress on slip plane

$\dot{g}^{\alpha}$ - Critical shear stress on each slip system

$h(\Gamma)$ - Hardening modulus

$\mathbf{L}$ - Velocity gradient

$\mathbf{L}^{p}$ - Plastic velocity gradient

m - Rate sensitivity exponent

$\mathbf{m}^{\alpha}$ - Slip plane normal

$q_{\alpha\alpha}$, $q_{\alpha\beta}$ - Hardening coefficients

$\mathbf{S}$ - 2nd Piola-Kirchhoff stress tensor

$\mathbf{s}^{\alpha}$ - Slip direction

Contents

List of Figures

List of Tables

1 Introduction

During the recent years, an increasing interest in metal additive manufacturing (AM) has occurred in both industry and research. This is due to the benefits of the processes, which include performance improvement and its ability to produce complex geometries (Kok et al., 2018). AM generates three-dimensional designs by coupling materials in a layer-by-layer process, where for instance metals and components of alloys can be created. There are a variety of different technologies that could be executed for creating AM metals, including sheet lamination, powder bed fusion and directed energy deposition. These components can then be used in several industries that require load-carrying structural elements, such as in aerospace. However, to fully utilize the metals created by AM, it is important to have significant knowledge of the microstructure.

The microstructure influences the engineering properties on macroscopic level, therefore it plays an important role in understanding the material behavior. By analyzing a component on microscale, a connection can be drawn to the macroscale through multiscale modelling (Wei et al., 2022). One way to implement this method is by using a representative volume element (RVE), which represents a significantly large part of the microstructure. This is important, because the RVE must be able to statistically represent the microstructure. An illustration of this is depicted in figure 1.1, which shows a metal beam with a part of its microstructure.

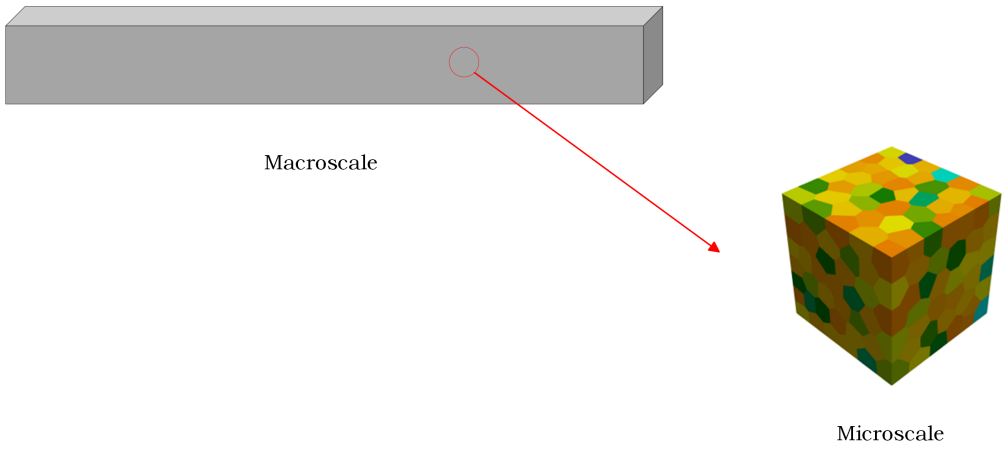

Figure 1.1: *A macroscale beam with a part of its microstructure represented by an RVE.*

In order to predict the material properties of AM metals, several software tools can be applied. Neper is an open-source software, where different grain morphologies can be generated (Quey & Kasemer, 2022). With Neper, it is possible to build models of microstructures similar to those obtained in additive manufacturing. To predict the mechanical properties of the microstructure represented by the RVE, crystal plasticity finite element method (CPFEM) is frequently applied. However, current research at Chalmers has provided an additional method through self-consistent based codes, which can be used to predict these characteristics without using FEM.

1.1 Aim and objectives

The aim of this thesis is to evaluate the elastic and plastic behavior of the additively manufactured Nickel-based alloys, Alloy 718 and Alloy 720Li, for different grain morphologies created in Neper. The analysis will be done at two different microscopic levels. The material response will be evaluated for each grain in the RVE, in addition to the entire RVE itself. This will be accomplished by using two different methods: CPFEM and a method with its origin in Eshelby's self-consistent model, where

the latter has been developed through research at Chalmers. The results from the two modeling approaches will then be compared with regards to accuracy and computational time.

1.2 Limitations

Since multiscale modelling of additively manufactured metals has gained attention the past few years, there is a lot to be done in terms of research. Therefore, several limitations will be applied to ensure that this study is completed within the decided time span, whilst sustaining a complexity fit for a master's thesis.

The following list presents the applied restrictions:

- **Material** - Various metals and alloys can be created with additive manufacturing. However, this study will focus on Alloy 718 and Alloy 720Li.
- **Mechanical properties** - Mechanical properties such as fatigue strength, can be analyzed for AM metals. In this project, the properties examined will be limited to elasticity and plasticity during monotonic loading.
- **Microstructure** - Equiaxed and elongated grains will be reviewed, no analysis will be made on a mixed grain structure.
- **Modelling** - The analysis will be limited to the microscale and the homogenization to macroscale behavior. Therefore, a full multiscale modelling procedure will not be implemented.

1.3 Method

To structure the work and make it achievable, a number of steps are implemented. This includes studying literature on the topic and implementing a numerical procedure to solve the project tasks.

1.3.1 Literature and software study

Since several software's will be used in this thesis, the first step is to learn the different softwares, with focus on ABAQUS and Neper. This is done by running simple models in ABAQUS with grain morphologies created in Neper. ABAQUS will be used for the FEM part of the project. The different commands in both applications are studied to be able to extract the best implementation for solving the actual problem further along in the project. Simultaneously, a literature study is conducted on the topic, including superalloy microstructures and crystal plasticity.

1.3.2 Numerical analysis

After the relevant information is gathered, a numerical analysis is applied to extract the elastic and plastic properties for the nickel-based superalloy. This is done by creating RVE:s in Neper for different grain morphologies by utilizing the knowledge from the software study. The CPFEM analysis is conducted in ABAQUS, whilst the self-consistent based software is written in Julia. In order to compare the results from the two methods, the following topics will be analyzed:

- How many grains are needed in the volume element to get a representative result?
- How fine mesh is needed to get converged results?
- How will the overall (homogenized) stress-strain behavior be for different microstructures?
- How does the individual grains behave and how will texture develop during loading?

2 Multiscale modelling of alloys

Implementing a multiscale procedure for metals includes modelling the material at different scales (Geers et al., 2017). In a simplified procedure, this could include two levels: macroscopic and microscopic. Generally, the goal of multi-level-modelling is to predict the mechanical properties on the macrolevel, by simulations of the underlying microstructure. On the microscale, the material response is heterogeneous, which will affect the stress and strain responses on the macroscopic scale. In order to understand the influence of the microstructure, a link between the different scales needs to be applied. Homogenization is a method that is commonly utilized for solving multiscale problems (March et al., 2023). With the microstructure as a foundation, a computational homogenization procedure can be implemented to predict the effective material response on higher scales. An illustration of this is exemplified in figure 2.1, where the stress-strain response of a beam has been extracted from the microstructure by implementing multiscale modelling.

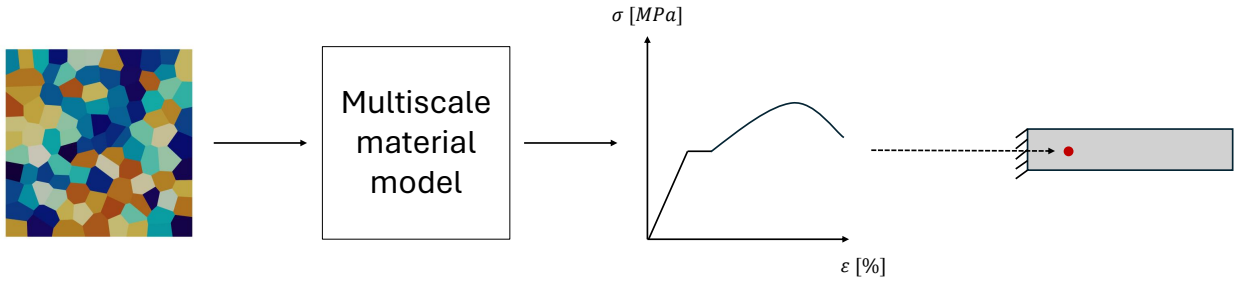

Figure 2.1: *Representation of multiscale modelling process. The figure depicts how a part of the microstructure can result in the stress-strain response in a macroscopic beam by using a multiscale material model.*

In this thesis, the focus will be on the microstructure. Different RVE:s will be generated and analyzed, in addition to analyzes on each grain of the RVE:s. However, there will be no full multiscale modelling procedure, as homogenization will only be made on the RVE. In order to understand the sub-scale, this chapter will focus on the morphology of the microstructure for additively manufactured alloys.

2.1 Microstructure of additvley manufactured alloys

Metals and alloys are typically polycrystalline. On the microstructural level, a polycrystalline metal consists of several grains that are separated by grain boundaries (Mouritz, 2012). Each grain has its own crystallographic orientation which can be further examined by analyzing the atomic structure. Within each grain, the arrangement of the atoms is essentially identical. However, since the direction of each grain is distinctive, the atomic configuration will vary for the grains. A simplification of this is illustrated in figure 2.2 which presents a two-dimensional surface of an RVE in the xy-plane. The arrows show the alignment of each grain, where two grains have been highlighted. The red lines represent the grain boundaries and the atomic structure of each grain is displayed regarding the direction of the grains.

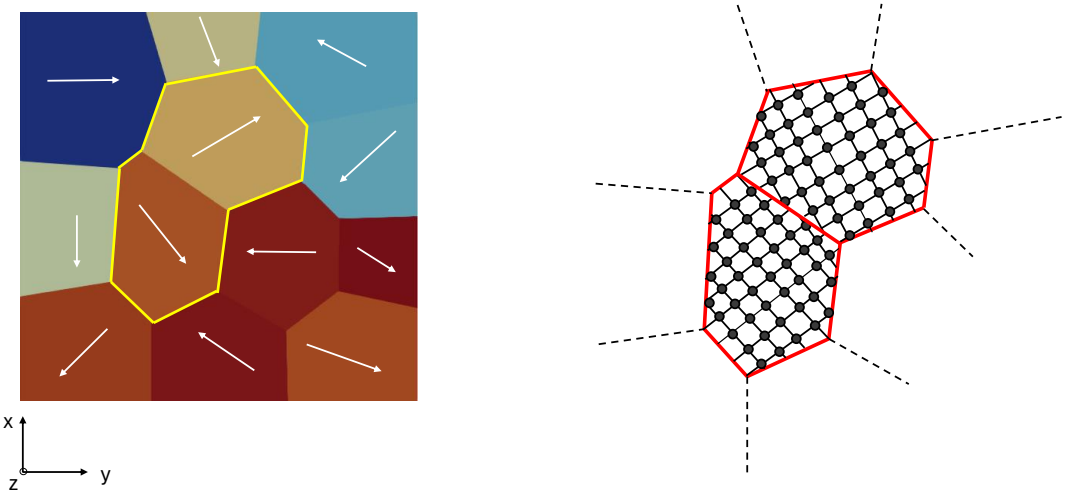

Figure 2.2: *2D illustration of grains with individual crystal orientations. The highlighted grains depict the grain boundaries and atomic arrangement.*

In AM, the metal solidification can be performed with powder bed fusion (PBF) processes which includes melting a bed of metallic powder with a radiative thermal source in a layer-by-layer process. As the metal solidifies, grains are created in a similar alignment as the thermal source (Dreelan et al., 2023). Through this process, the grain orientations, known as the crystallographic texture are created. In contrast to metals made by casting, AM metals created through laser powder bed fusion tend to have finer microstructures with either columnar, equiaxed or mixed grain structure (Narayana Samy et al., 2023). In this report, columnar and equiaxed grains will be further examined and how they affect macroscopic material properties.

2.2 Grain morphologies

The grain composition is mainly determined by two parameters, the solidification rate (R) which describes how fast each layer solidifies, and the local temperature gradient (G) which is the absolute value between the liquid and the metal during solidification (Hagenlocher et al., 2022). Since AM creates metals and alloys in a layer-by-layer fashion, the grain structure of each separate layer is affected locally by the mentioned parameters.

In order to obtain columnar grains, low G/R ratios at the base of the melting bed is necessary (Narayana Samy et al., 2023). Columnar grains are elongated in the build direction, with favoured <001> crystal orientation, which results in textured grains and a anisotropic material response on the macroscopic scale (Eshragi & Yoshioka, 2023), (Gundgire et al., 2020). This may prove to be unfavorable when load is applied to the specimen. Additionally, elongated grains result in large grain boundaries, which are vulnerable to crack initiation (Li, Huang, et al., 2021). However, there are several advantages of anisotropy, one being enhanced creep resistance. In figure 2.3 a variant of a columnar microstructure is depicted as an RVE. The grains are elongated in the build direction (z-axis), which gives different grain structures in different planes, as shown in the figure.

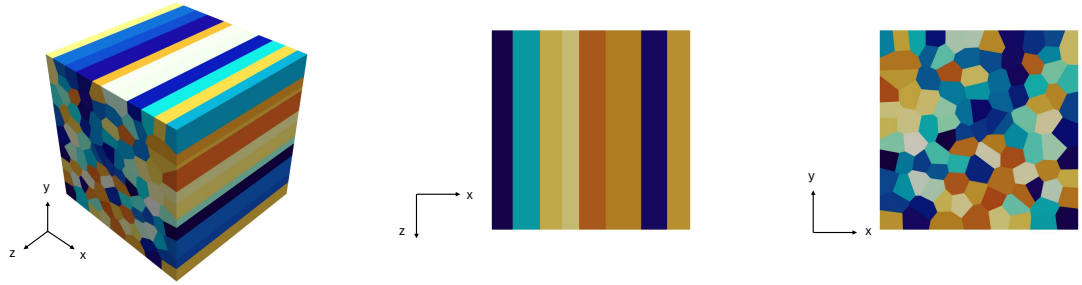

Figure 2.3: *Representation of a columnar microstructure by an RVE, with a two-dimensional representation i the xz plane and the xy plane. The RVE is created in Neper and consists of 100 grains.*

Equiaxed grains can be obtained during the solidification process, where the columnar to equiaxed transition can occur (CET) as a result of heterogeneous nucleation or through different G/R ratios (Narayana Samy et al., 2023). However, modifying the G/R ratio tends to be a complicated process. The procedure of nucleation is that a master alloy is added to the melting bed, with the purpose of creating a new structure of the grains (Greer, 2016). Through this approach, the growth of columnar grains is prevented, and an equiaxed grain structure is the result.

The material behavior (on the macroscopic scale) of equiaxed grains is isotropic, which is an advantage in different aspects (Gundgire et al., 2020). Equiaxed grains have randomized crystallographic orientation and therefore weak texture that indicate isotropy, which contributes to a more homogenized microstructure (Todaro et al., 2020). Unlike columnar grains, equiaxed grains have increased resistance to crack propagation and fatigue life (Li, Huang, et al., 2021). An illustration of an RVE with equiaxed grains is shown in figure 2.4 in addition to the surface in the xz plane. Since the grains are equiaxed, the dimensions are similar in all directions. Therefore the microstructure will look similar in all planes.

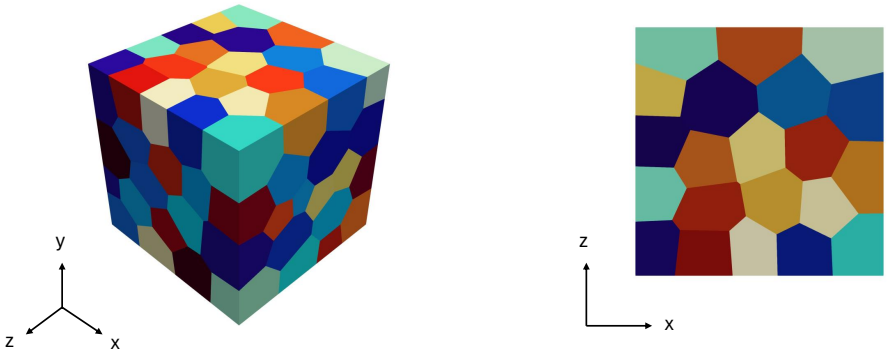

Figure 2.4: *Representation of an equiaxed microstructure by an RVE, with a two-dimensional representation in the xz plane. The RVE is created in Neper and consists of 100 grains.*

Columnar and equiaxed microstructures have grains with different crystal orientations, making them anisotropic on the micro-scale. If the crystal orientations are random, the macroscopic response tends to be isotropic, which is the case for equiaxed grains (Kumara et al., 2018). Meanwhile, columnar grains are textured and are therefore anisotropic.

2.3 Nickel-based superalloys

The Nickel-based superalloy 718, often referred to as Inconel 718 (IN718), is commonly used in gas turbines and jet engines due to its ability to exhibit strong material properties at high temperatures (Zhong et al., 2019). IN78 is composed of different metal elements with the weight percentage presented in table 2.1. Usually, the grain structure of Alloy 718 is columnar (Gundgire et al., 2020). However as discussed in chapter 2.2, equiaxed grain morphologies are possible to obtain.

Table 2.1: *Chemical composition of Alloy 718 in weight percent.*

Metal elements for Alloy 718 in wt%								
Ni	**Cr**	**Fe**	**Nb**	**Mo**	**Mn**	**Al**	**Ti**	**Co**
50.0–55.0	17.0–21.0	Balance	4.75–5.50	2.8–3.3	<0.35	0.2–0.8	0.65–1.15	<1.0

Additionally, Alloy 720Li also performs well under high temperatures and is therefore used in gas turbines (Daymond et al., 2007). In contrast to IN718, Alloy 720Li is a two-phase material, which means that the material properties will vary for the grains based on the volume fractions. The weight percent of phase 1 is 55%, while 45% weight percent is phase 2. The material composition of Alloy 720Li is presented in table 2.2.

Table 2.2: *Chemical composition of Alloy 720Li in weight percent.*

Metal elements for Alloy 720Li in wt%								
Cr	**Co**	**Mo**	**W**	**Al**	**Ti**	**C**	**B**	**Ni**
18	15	3.0	1.25	2.5	5.0	0.020	0.032	Balance

The matrix phase of both alloys, γ, is a Face-Centred Cubic (FCC) crystal formation (Zaikovska et al., 2023). Here, γ represents the material in question. An FCC crystal consists of a cubic cell with atoms at each corner in the cube, in addition to atoms in the centres of each face of the crystal (Flowers et al., 2015). Since these cubic cells are connected to one another in crystalline structures, they share atoms. Therefore, one FCC unit cube consists of four atoms in total: $\frac{1}{8}$th atom at each corner and $\frac{1}{2}$th atom at each face. Because of this, each side of the cube is identical. This is exemplified in figure 2.5, by examining at the crystal structure of the grains in figure 2.2. The black spheres represent the atoms at each corner of the unit cube, while the blue spheres represent the atoms at the face.

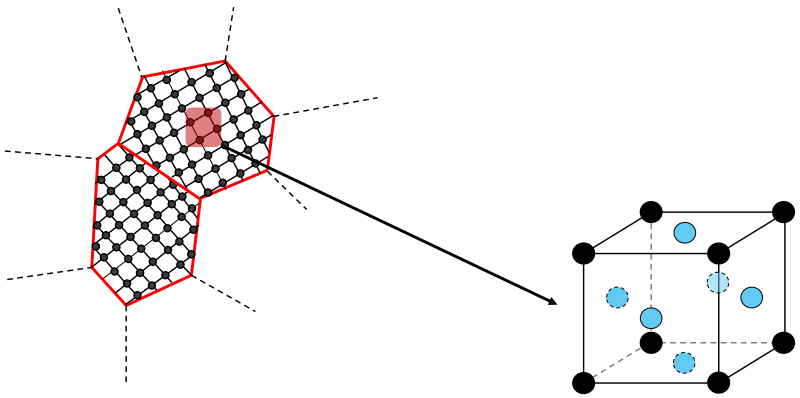

Figure 2.5: *Illustration of an FCC crystal in a crystalline grain structure.*

3 Crystal elasticity and plasticity

Since Alloy 718 is a polycrystalline metal, the mechanical response of AM metals on the microscale can be modelled by cubic elasticity and crystal plasticity. In this chapter, a brief summary of these models will be presented.

3.1 Euler-Bunge angles

As discussed and illustrated in chapter 2, a polycrystalline metal consists of grains, where each grain is considered as a crystal with a certain orientation. The crystallographic orientations can be described by using Euler angles with the Bunge convention (Bunge, 1982). In order to describe the rotation of the crystal, an arbitrary coordinate system of the specimen, can be defined. The coordinate system can be described by the orthogonal normal vectors $\boldsymbol{e}_x, \boldsymbol{e}_y, \boldsymbol{e}_z$, which is illustrated in figure 3.1a (Kelly & Knowles, 2020). The crystal vectors is described with the crystal fixed coordinate system $\boldsymbol{e}_x^{'}, \boldsymbol{e}_y^{'}, \boldsymbol{e}_z^{'}$. From figure 2.5, it can be recalled that a crystal is built up of unit cells, which describes the rotated coordinate system in figure 3.1b.

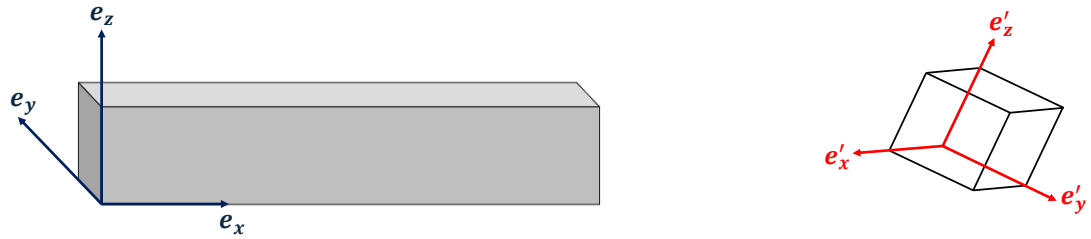

(a) **(b)**

Figure 3.1: *Coordinate systems on different scales. (a) presents the coordinate system $\boldsymbol{e}_x, \boldsymbol{e}_y, \boldsymbol{e}_z$ for the specimen on the macroscale, while (b) represents the oriented coordinate system $\boldsymbol{e}_x^{'}\boldsymbol{e}_y^{'}\boldsymbol{e}_z^{'}$ of a unit cell.*

To obtain the crystal orientation in terms of Euler-Bunge angles, three rotations are defined, where the crystal starts by having the same coordinate system as the specimen (Kelly & Knowles, 2020). Firstly, a rotation φ_1 around the $\boldsymbol{e}_z$-axis is defined which results in the base vectors $\boldsymbol{e}_x^{(1)}$, $\boldsymbol{e}_y^{(1)}$, $\boldsymbol{e}_z^{(1)}$. Therafter, a second rotation Φ is made around the $\boldsymbol{e}_x^{(1)}$-axis, which results in the base vectors $\boldsymbol{e}_x^{(2)}$, $\boldsymbol{e}_y^{(2)}$, $\boldsymbol{e}_z^{(2)}$. The last rotation φ_2 is around the rotated axis $\boldsymbol{e}_z^{(2)}$, which results in the final coordinate system $\boldsymbol{e}_x^{'}\boldsymbol{e}_y^{'}\boldsymbol{e}_z^{'}$. The rotations of the coordinate system are presented in figure 3.2, where (a), (b) and (c) represent the first, second and third rotation, respectively. This procedure can also mathematically be described with three rotation matrices. The rotated coordinate system due to φ_1 is described by (3.1), while (3.2) presents the coordinate system as a result of the rotation around the $\boldsymbol{e}_x^{(1)}$-axis. Lastly, (3.3) shows the calculation for the final coordinate system. The rotations can vary between [0, 360°] for φ_1 and φ_2 , while Φ ranges between [0, 180°] (Chen et al., 2022).

$$\begin{bmatrix}\mathbf{e}_x^{(1)} & \mathbf{e}_y^{(1)} & \mathbf{e}_z^{(1)}\end{bmatrix} = \begin{bmatrix}\mathbf{e}_x & \mathbf{e}_y & \mathbf{e}_z\end{bmatrix} \begin{bmatrix}\cos\varphi_1 & -\sin\varphi_1 & 0 \\ \sin\varphi_1 & \cos\varphi_1 & 0 \\ 0 & 0 & 1\end{bmatrix} = \begin{bmatrix}\mathbf{e}_x & \mathbf{e}_y & \mathbf{e}_z\end{bmatrix} \begin{bmatrix}\mathbf{R}_{\varphi_1}\end{bmatrix} \tag{3.1}$$

$$\begin{bmatrix}\mathbf{e}_x^{(2)} & \mathbf{e}_y^{(2)} & \mathbf{e}_z^{(2)}\end{bmatrix} = \begin{bmatrix}\mathbf{e}_x^{(1)} & \mathbf{e}_y^{(1)} & \mathbf{e}_z^{(1)}\end{bmatrix} \begin{bmatrix}1 & 0 & 0 \\ 0 & \cos\Phi & -\sin\Phi \\ 0 & \sin\Phi & \cos\Phi\end{bmatrix} = \begin{bmatrix}\mathbf{e}_x^{(1)} & \mathbf{e}_y^{(1)} & \mathbf{e}_z^{(1)}\end{bmatrix} \begin{bmatrix}\mathbf{R}_{\mathbf{\Phi}}\end{bmatrix} \tag{3.2}$$

$$\begin{bmatrix} \mathbf{e}_x' & \mathbf{e}_y' & \mathbf{e}_z' \end{bmatrix} = \begin{bmatrix} \mathbf{e}_x^{(2)} & \mathbf{e}_y^{(2)} & \mathbf{e}_z^{(2)} \end{bmatrix} \begin{bmatrix} \cos\varphi_2 & -\sin\varphi_2 & 0 \\ \sin\varphi_2 & \cos\varphi_2 & 0 \\ 0 & 0 & 1 \end{bmatrix} = \begin{bmatrix} \mathbf{e}_x^{(2)} & \mathbf{e}_y^{(2)} & \mathbf{e}_z^{(2)} \end{bmatrix} \begin{bmatrix} \mathbf{R}_{\varphi_2} \end{bmatrix} \tag{3.3}$$

In conclusion, the conversion from $\mathbf{e}_x\mathbf{e}_y\mathbf{e}_z$ to $\mathbf{e}_x'\mathbf{e}_y'\mathbf{e}_z'$, can be described by matrix multiplication of the three rotation matrices in accordance with (3.4).

$$\begin{bmatrix} \mathbf{e}_x' & \mathbf{e}_y' & \mathbf{e}_z' \end{bmatrix} = \begin{bmatrix} \mathbf{e}_x & \mathbf{e}_y & \mathbf{e}_z \end{bmatrix} \mathbf{R}_{\varphi_1}\mathbf{R}_{\mathbf{\Phi}}\mathbf{R}_{\varphi_2} \tag{3.4}$$

To describe the total rotation matrix, $\mathbf{R}$, of the crystal, the multiplication of the three transposed rotation matrices is made (3.5).

$$\begin{aligned} \mathbf{R} &= (\mathbf{R}_{\varphi_1}\mathbf{R}_{\mathbf{\Phi}}\mathbf{R}_{\varphi_2})^T = \mathbf{R}_{\varphi_2}^T\mathbf{R}_{\mathbf{\Phi}}^T\mathbf{R}_{\varphi_1}^T = \\ &= \begin{bmatrix} \cos\varphi_1\cos\varphi_2 - \sin\varphi_1\cos\Phi\sin\varphi_2 & \sin\varphi_1\cos\varphi_2 + \cos\varphi_1\cos\Phi\sin\varphi_2 & \sin\Phi\sin\varphi_2 \\ -\cos\varphi_1\sin\varphi_2 - \sin\varphi_1\cos\Phi\cos\varphi_2 & -\sin\varphi_1\sin\varphi_2 + \cos\varphi_1\cos\Phi\cos\varphi_2 & \sin\Phi\cos\varphi_2 \\ \sin\varphi_1\sin\Phi & -\cos\varphi_1\sin\Phi & \cos\Phi \end{bmatrix} \end{aligned} \tag{3.5}$$

As mentioned in chapter 2.2, equiaxed grains have random orientation, while elongated grains tend to have <001> orientation. In terms of Euler angles, this means that equiaxed grains are rotated for all angles φ_1 , ϕ , φ_2 . However, the <001> orientation for columnar grains implies that there is only a rotation around the $\mathbf{e}_z$-axis, thus, φ_1 is the only non-zero angle.

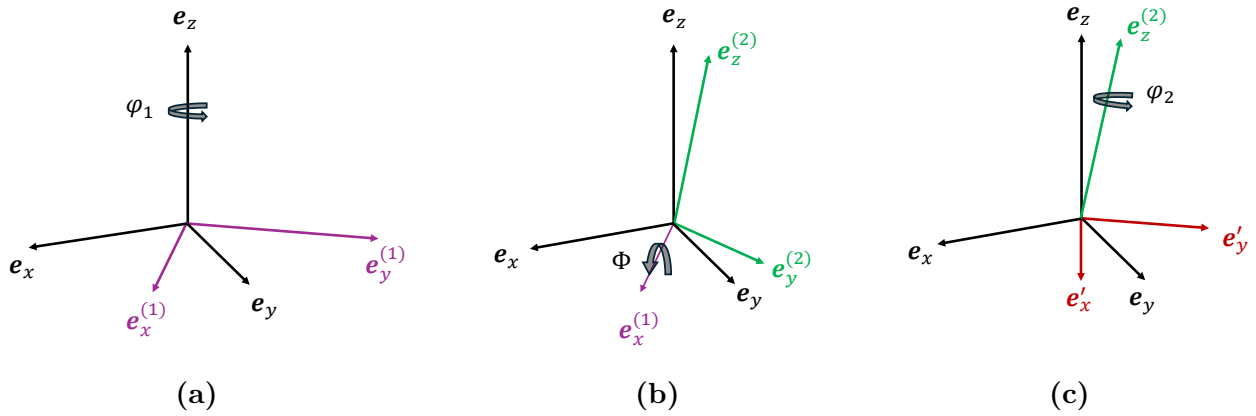

Figure 3.2: *Representation of rotations with Euler-Bunge angles with regards to a reference coordinate system: (a) first rotation, φ_1, (b) second rotation, Φ, (c) third rotation, φ_2.*

3.2 Pole figures

Pole figures can be used to graphically represent the crystal orientations described by Euler angles (Tomé & Lebensohn, 2023). This can be done by taking a grain from the microstructure and imagining its crystal orientation in the center of a sphere. By examining the sphere in different planes, a two-dimensional representation can be obtained and the result is a pole figure. To exemplify this, it is possible to look from the north pole of the sphere and examine an intersecting plane, similar to what is presented in figure 3.3. Here, the intersecting plane is marked in red, while the highlighted grain represents the crystal orientation. In this example, the crystal directions are projected on the plane in three places, which are marked in blue in the figure. By implementing the same procedure for all grains, the crystal orientations of all the grains in an RVE for a specific slip system can be added to the pole figure, as seen in figure 3.3.

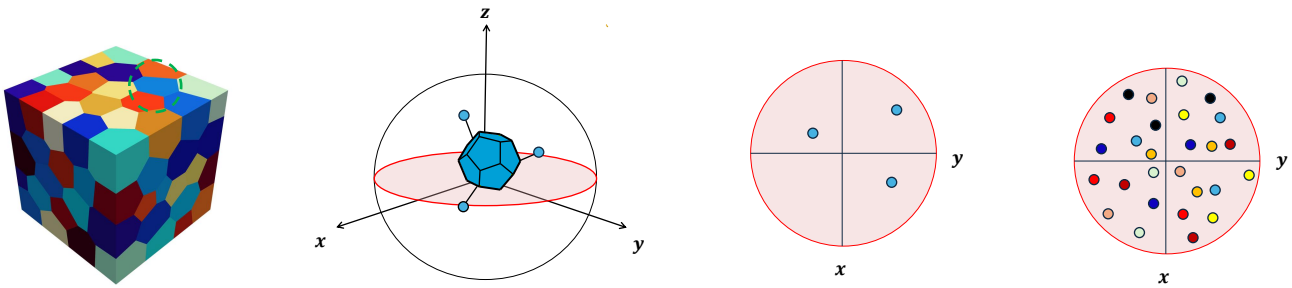

Figure 3.3: *Illustration of pole figures for one specific crystal orientation and for several different orientations.*

3.3 Elastic cubic symmetry

Generally, the elastic stress-strain behavior of a single cubic crystal is described in tensor form according to (3.6) (Kelly & Knowles, 2020). Besides the crystal orientation given by the Euler angles, three additional material parameters are required for defining linear elasticity of cubic crystals (Chen et al., 2022). These are the stiffness constants C_{11}, C_{12} and C_{44}. The fourth order stiffness tensor is presented in Voigt form (in the crystal fixed coordinate system) in (3.7) and contains the three stiffness constants. Through this definition, the response under elastic strains can be described.

$$\sigma_{ij} = C_{ijkl}\varepsilon_{kl} \tag{3.6}$$

$$\mathbb{C} = [C_{ijkl}] = \begin{bmatrix} C_{11} & C_{12} & C_{12} & 0 & 0 & 0 \\ C_{12} & C_{11} & C_{12} & 0 & 0 & 0 \\ C_{12} & C_{12} & C_{11} & 0 & 0 & 0 \\ 0 & 0 & 0 & C_{44} & 0 & 0 \\ 0 & 0 & 0 & 0 & C_{44} & 0 \\ 0 & 0 & 0 & 0 & 0 & C_{44} \end{bmatrix} \tag{3.7}$$

3.4 Crystal plasticity

Plasticity occurs when an applied stress is large enough to cause permanent deformation (Kelly & Knowles, 2020). Plasticity is induced by shear stresses, which results in gliding between atoms in the crystal lattice, which remains undistorted during yielding. Gliding is defined by two parts of a crystal moving relatively to each other, while maintaining constant volume. This can be presented in a simplified matter through figure 3.4a, which illustrates a single crystal prior to plastic deformation, while figure 3.4b presents the gliding due to shear. If the imposed shear stress is not significant enough to cause plasticity, gliding does not occur and the crystal will deform elastically.

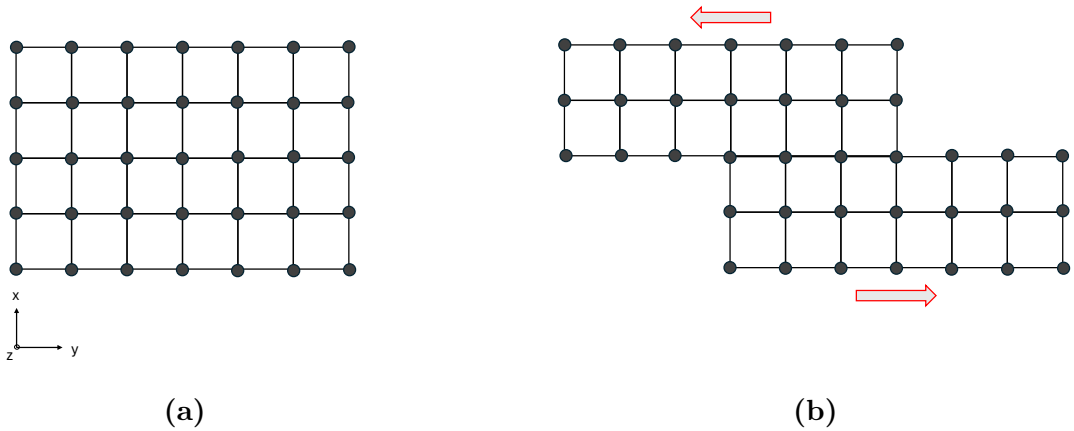

(a) **(b)**

Figure 3.4: *Plastic response of a single crystal. The crystalline structure is depicted before loading (a) and after applied shear force (b).*

3.4.1 Slip systems

To elaborate on the definition of gliding, slip occurs on a crystal plane in a particular direction (Yang & Park, 2003). As mentioned, this occurs due to shear stress and results in two parts of the crystals moving relatively to one another. The crystal plane is often referred to as the *slip plane*, while the direction in which it occurs is denoted as the *slip direction*. The slip plane and the slip direction, together make up the *slip system*. Slip is more vulnerable on certain directions than others. Since slip is caused by shear, the critical resolved shear stress (CRSS) value, τ_α, can be described by *Schmid's law* (3.8). Where σ, is the applied uniaxial stress. The angle between the applied load direction and the slip direction is expressed by ϕ, while λ is the angle between the applied load direction and the normal of the slip plane.

$$\tau_\alpha = \sigma \, cos\phi \, cos\lambda \tag{3.8}$$

Depending on the characteristics of the crystal, a certain number of slip systems are possible (Yang & Park, 2003). The FCC crystal structure has 12 slip systems in total, which is characterized by the <1,1,0> slip direction and a {111} slip plane. In the {111} plane category, four different slip planes can be identified: (111), ($\bar{1}$11), (1$\bar{1}$1) and (11$\bar{1}$) (Sun et al., 2020). The coordinates are given by Miller indices, where a line over a number indicates a negative value, thus $\bar{1}$ = -1. Each slip plane has three different slip directions, hence 4x3=12 slip systems, all of which are presented in table 3.1. The slip plane, $\boldsymbol{m}^\alpha$, and slip direction, $\boldsymbol{s}^\alpha$, are normalized (Zhang et al., 2021), (Dequiedt, 2018). For clarification, an illustration of the slip plane (111) for a FCC unit cell is presented in figure 3.5. The three slip systems associated with the slip plane in table 3.1, are visualized in figure 3.5 with regards to the presented coordinate system.

Table 3.1: *Slip systems for a FCC crystal, and their related slip plane and slip directions. The values are normalized.*

Slip system α	Slip plane normal, $\mathbf{m}_0^\alpha$	Slip direction vector, $\mathbf{s}_0^\alpha$
1	$(111)/\sqrt{3}$	$[\bar{1}10]\sqrt{2}$
2		$[10\bar{1}]\sqrt{2}$
3		$[0\bar{1}1]\sqrt{2}$
4	$(\bar{1}11)/\sqrt{3}$	$[101]\sqrt{2}$
5		$[110]\sqrt{2}$
6		$[0\bar{1}1]\sqrt{2}$
7	$(1\bar{1}1)/\sqrt{3}$	$[011]\sqrt{2}$
8		$[110]\sqrt{2}$
9		$[10\bar{1}]\sqrt{2}$
10	$(11\bar{1})/\sqrt{3}$	$[011]\sqrt{2}$
11		$[101]\sqrt{2}$
12		$[\bar{1}10]\sqrt{2}$

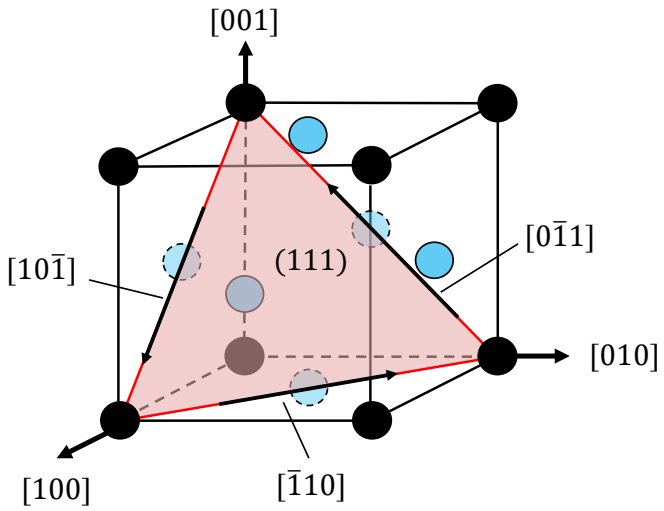

Figure 3.5: *Representation of the slip plane (111) with its corresponding slip systems for an FCC unit cells. Note: the slip planes and directions are not normalized in the figure.*

3.5 Theoretical model

To describe crystal plasticity in terms of material mechanics, a theoretical model needs to be presented (Segurado & Llorca, 2013). This can then be implemented in the numerical analysis. The material model is usually presented in terms of large deformations. However, in this report, the model will be presented for small deformations to simplify for the reader. Although the stress-strain behavior can be presented in terms of small deformations, the texture development during loading can only be described by large deformations. Therefore, the material model for large deformations is presented in Appendix B.

The plastic deformation occurs on multiple slip planes, where the plastic strain rate, $\dot{\boldsymbol{\varepsilon}}^p$, can be calculated by summing the shear rates, $\dot{\gamma}^\alpha$, of each slip system α (3.9).

$$\dot{\boldsymbol{\varepsilon}}^p = \sum_{\alpha=1}^{n} \dot{\gamma}^\alpha \ (\mathbf{s}_0^\alpha \otimes \mathbf{m}_0^\alpha)^{\text{sym}} \ \frac{\tau^\alpha}{|\tau^\alpha|} \tag{3.9}$$

Further, it is assumed that the crystals have an elasto-viscoplastic material response. Therefore the shear rate, also referred to as the plastic slip rate, can be described according to (3.10) for each slip system. Here, $\dot{\gamma}_0$ represents the reference shear strain rate, while g^α is the critical stress on the slip system. Furthermore, τ^α is the resolved shear stress and m defines the rate-sensitivity exponent.

$$\dot{\gamma}^\alpha = \dot{\gamma}_0 \left(\frac{|\tau^\alpha|}{g^\alpha} \right)^{\frac{1}{m}} sign(\tau^\alpha) \tag{3.10}$$

Through the traction vector $\mathbf{t}_0^\alpha$ and the slip normal $\mathbf{m}_0^\alpha$, the resolved shear stress, τ^α can be obtained by projecting the stress, σ, on the slip system, which is described by $\mathbf{s}_0^\alpha \otimes \mathbf{m}_0^\alpha$ (3.11).

$$\tau^\alpha = \mathbf{t}_0^\alpha \cdot \mathbf{s}_0^\alpha = \sigma : (\mathbf{s}_0^\alpha \otimes \mathbf{m}_0^\alpha) \tag{3.11}$$

From the expression (3.12), it is possible to define the evolution of the critical shear stress of each system. The hardening modulus is defined by $h(\gamma)$, while $q_{\alpha\beta}$ represents the hardening coefficient that considers the impact from the other slip systems. The hardening coefficient for the slip system in question is represented by $q_{\alpha\alpha}$. Here, γ is the accumulated plastic shear strain on all the active slip systems, as defined by (3.13). To define the hardening modulus, $h(\gamma)$, Voce hardening model is applied for single crystals (3.14). In this expression, h_0 and h_s describe the initial and the saturation hardening respectively, while τ_s represents the saturation shear stress. In addition, to describe hardening in this model, the initial critical shear stress, $g^\alpha(\gamma = 0) = \tau_0$, needs to be defined.

$$\dot{g}^\alpha = q_{\alpha\alpha} \, h(\gamma) \, \dot{\gamma}^\alpha + \sum_{\beta \neq \alpha} q_{\alpha\beta} \, h(\gamma) \, \dot{\gamma}^\beta \tag{3.12}$$

$$\gamma = \sum_\alpha \int |\dot{\gamma}^\alpha| dt \tag{3.13}$$

$$h(\gamma) = h_0 + \left(h_0 - h_s + \frac{h_0 h_s \gamma}{\tau_s} \right) e^{-h_0 \gamma / \tau_s} \tag{3.14}$$

4 Numerical implementation

CPFEM and J-AMEN are two different homogenization methods for predicting the macroscopic material response during loading, and therefore the implementation techniques deviate from each other, as presented in figure 4.1. For CPFEM, several steps need to be performed before results can be obtained. Firstly, the desired grain morphologies with their crystal orientations need to be created and meshed in Neper. Thereafter, user-defined scripts for the crystal plasticity material model (UMAT) and boundary conditions (DISP) need to be created and plugged into Abaqus for the simulations. The simulations are done on the cluster provided by C3SE. The results are extracted by Python scripting and the post-processing for the homogenization is done in MATLAB. For J-AMEN, the procedure is different. While CPFEM requires the meshed RVE, J-AMEN only needs the Euler angles and number of grains from Neper. This can then be inserted into the code containing the material model, written in Julia, after which results are almost instantly given (1-2 minutes). In this chapter, an overview of the different steps for the two methods will be presented, and an explanation of J-AMEN software will be provided.

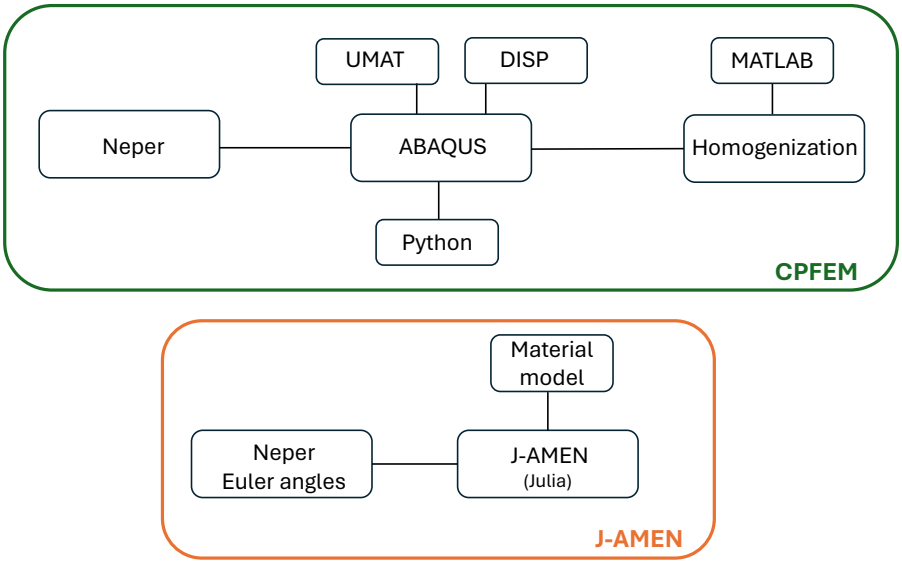

Figure 4.1: *Necessary steps for implementing CPFEM and J-AMEN. In this figure, the necessary steps for CPFEM are marked in green, while steps marked in orange represent J-AMEN.*

4.1 Generation of grain morphologies

Neper is an open-source software where Voronoi tessellation can be used to generate models for grain structures and then mesh them (Quey & Kasemer, 2022). In other words, Neper creates the RVE's for different microstructures. Since equiaxed and elongated grains are to be examined in this project, the settings in Neper need to be adjusted to fit the desired grain structure. This is done in the "Tessellation module", *-T*. The 3D representations of the microstructure are then meshed in the "Mesh module", *-M*. In this step, an input file for the mesh can be created and used for the simulations in ABAQUS. In Neper, each grain is meshed separately, i.e. the software does not mesh the entire RVE with respect to the chosen mesh size. In this report, the grains are meshed by deciding a *relative characteristic length* (rcl), that relates to the average grain size and results in a specific number of elements for each grain.

The equiaxed microstructure is created by controlling the diameter size and the sphericity of the grains. For the diameter, a lognormal distribution of mean 1 and standard deviation of 0.01 are chosen. Similarly, a lognormal distribution of the sphericity is decided with a mean value of 0.145 and standard deviation of 0.01. The low standard deviation ensures that the variation between grains is limited, which results in an equiaxed microstructure. Additionally, Euler angles with random orientation are specified for the grains. For elongated grains an aspect ratio is given, instead of diameter and sphericity. Microstructures with aspect ratios of 1:2 - 1:10 are created to get a description of the variation in the stress-strain behavior within elongated grains. The Euler angles are generated such that there is only a random orientation around the build direction, in this case the z-axis. However, the different grain morphologies are meshed correspondingly, with linear tetrahedral elements. In ABAQUS, this corresponds to C3D4 elements. In figure 4.2a, the meshed RVE for 500 equiaxed grains is presented. Similarly, 4.2b and 4.2c present elongated grains with aspect ratio 1:2 and 1:5 respectively, for the same number of grains.

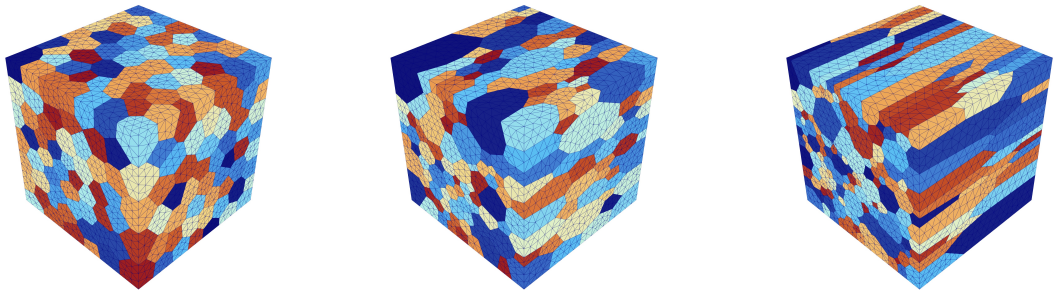

(a) **(b)** **(c)**

Figure 4.2: *Generated RVE's in Neper with 500 grains for the following grain morphologies: (a) equiaxed, (b) elongated with aspect ratio 1:2 (c) elongated with aspect ratio 1:5.*

4.2 Material model

To predict the material response for CPFEM, a material model needs to be defined. In ABAQUS, a built in material model for crystal plasticity does not exist and therefore it needs to be user defined. This is done through a UMAT-file, which is a Fortran script provided by the user for the desired material model (ABAQUS, 2006). In this case, the UMAT is defined in terms of large deformations. The UMAT used in this report has been created by Prof. Magnus Ekh, where equations (B.1)-(B.9) from the theoretical model in Appendix B have been implemented. For this UMAT, it is necessary to define 14 material parameters. This includes the three Euler angles of each grain, and the elastic stiffness constants discussed in chapter 3.3. Additionally, the material parameters for plasticity presented in Appendix B need to be defined (it should be noted that the corresponding material parameters for a small deformation crystal plasticity model are given in chapter 3.5).

As previously stated, the Euler angles will be different for all grains regardless of the grain structure. However, for Alloy 718 the material parameter values are identical for all grains and are presented in table 4.1. Similarly, the material parameter values for the two phases of Alloy 720Li are disclosed in table 4.2, where the properties will vary based on the volume fractions as described in chapter 2.3. Therefore, 55% of the RVE's volume will correspond to phase 1, while phase 2 will be applied to the remaining grains. It should be noted that for the elastic analysis, the yield strength, τ_0, is set to a high value to ensure an elastic response. Also, $q_{\alpha\beta}$ will be equal to 0.99 for all analyses except for the texture development, where the value will be equal to 2. Now, in addition to the mesh input file from

Neper, an input file that contains the Euler angles and necessary material parameters for each grain can be created.

Table 4.1: *Material parameter values for Alloy 718. All values are given in MPa, except for $\dot{\gamma}_0$ which is in 1/s while m, $q_{\alpha\alpha}$ and $q_{\alpha\beta}$ are unitless.*

C11	C12	C44	$\dot{\gamma}_0$	m	h_s	h_0	τ_s	τ_0	$q_{\alpha\alpha}$	$q_{\alpha\beta}$
259 600	179 000	109 600	0.1	0.017	300	6000	598.5	465.5	1	0.99/2

Table 4.2: *Material parameter values for Alloy 720Li. All values are given in MPa, except for $\dot{\gamma}_0$ which is in 1/s while m, $q_{\alpha\alpha}$ and $q_{\alpha\beta}$ are unitless.*

Material	C11	C12	C44	$\dot{\gamma}_0$	m	h_s	h_0	τ_s	τ_0	$q_{\alpha\alpha}$	$q_{\alpha\beta}$
Phase 1	254 600	170 900	137 400	0.1	0.017	35	60	381	376	1	0.99/2
Phase 2	249 215	165 069.7	131 645.5	0.1	0.017	754	798	389	384	1	0.99/2

4.3 Virtual testing

In this report, virtual testing is used to understand the material response during loading. With virtual testing it is possible to control the boundary conditions on macroscale, such that the specimen only experiences load in one direction. This is illustrated in figure 4.3, where (a), (b) and (c) present the cases of pure tension, while (c), (d) and (e) represent the three cases of pure shear. In this thesis, the displacements will be controlled, such that all strains are equal to zero except for the prescribed strain. The strain will have the same magnitude on microscale. Similarly to UMAT, this procedure needs to be user defined for CPFEM through a Fortran script called DISP (ABAQUS, 2006). For the elastic analysis, a strain of 0.1% is applied for all directions. When studying plasticity, the strain is increased to 5% and for the texture analysis the strain is 20%. The final input file that describes the boundary conditions can now be created and the ABAQUS simulations can be done in the cluster. Virtual testing can also be performed with periodic boundary conditions. They have the benefit that a smaller volume element can be used to get a representative response but they are more difficult to implement in Abaqus. Hence, the virtual testing procedure with linearly varying displacements on the boundaries (as illustrated in figure 4.3) has been adopted in this thesis.

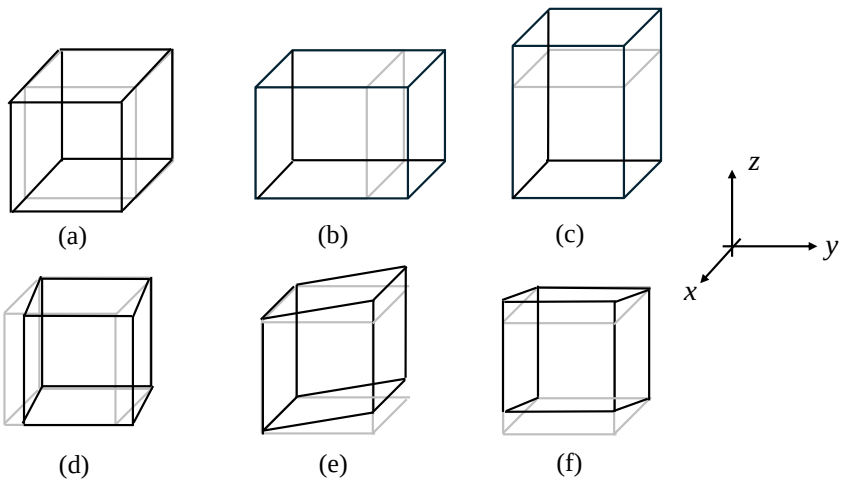

Figure 4.3: *Virtual testing cases, pure tension in: (a) x-direction, (b) y-direction, (c) z-direction. Virtual testing cases, pure shear in: (d) xy-direction, (e) xz-direction, (f) yz-direction*

4.4 Computational homogenization

From Abaqus, the results are extracted through Python scripting. For the computational homogenization, it is necessary to select the stresses (S), the strains (E, LE), the element volume (EVOL) and certain solution-dependent state variables (SDV) that are defined in the UMAT. Afterwards, the homogenization calculations are done in MATLAB for the entire RVE, in addition to each grain in the RVE. An illustration of the two different homogenization levels is presented in figure 4.4, where the separate notations for the homogenized stress and strain are introduced.

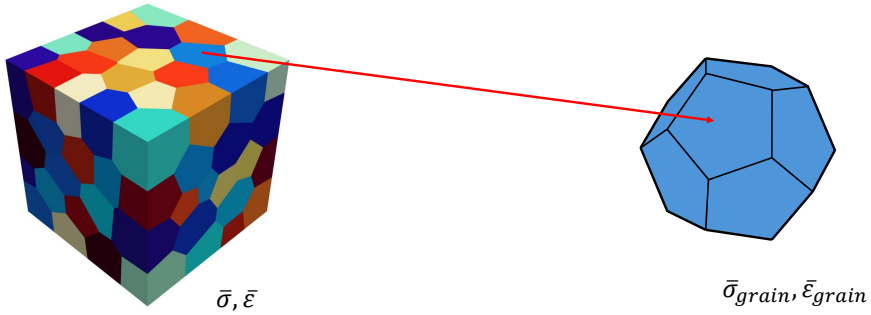

Figure 4.4: *Illustration of the two different homogenization levels, the RVE and the grains, that are examined in the thesis.*

4.4.1 RVE

The homogenization procedure for the entire RVE is conducted over the total volume of the cube, according to (4.1). Here, V_e is the element volume, and σ_e is the centroid stress in the corresponding element. By choosing the stress in the center of the element, it is ensured that an average element stress is extracted. The product of these values is then summed and divided with the complete volume of the RVE and the result is the homogenized stress, $\overline{\boldsymbol{\sigma}}$. This is applied for all the normal and shear stress components and results in an averaged stress over the specimen. Similarly, by exchanging the stress with the strain, an implementation of this procedure can be utilized to get an averaged strain distribution, $\bar{\varepsilon}$, for the RVE (4.2).

$$\overline{\boldsymbol{\sigma}} = \frac{1}{V} \sum_{e=1}^{n_{elem}} V_e \, \boldsymbol{\sigma}_e \tag{4.1}$$

$$\overline{\boldsymbol{\varepsilon}} = \frac{1}{V} \sum_{e=1}^{n_{elem}} V_e \, \boldsymbol{\varepsilon}_e \tag{4.2}$$

As mentioned, virtual testing is used for all analyses and ensures that the macroscopic strain is only applied one component at a time. It is especially useful for the elastic procedure as it allows for the homogenized stress-strain behavior to be described through the elastic stiffness tensor. This can be exemplified by the virtual testing case, $\bar{\varepsilon}_{11} \neq 0$. The first step is to assume the equation system in (4.3), which describes Hooke's law. After the stresses from ABAQUS have been extracted and homogenized, the $\overline{\sigma}$ values will be known. Additionally, the applied strain is known from the analysis and can also be homogenized to get $\bar{\varepsilon}$. Therefore, it is possible to solve for the homogenized stiffness tensor, $\overline{\mathbf{E}}$, column by column.

$$\begin{bmatrix} \overline{\sigma}_{11} \\ \overline{\sigma}_{22} \\ \overline{\sigma}_{33} \\ \overline{\sigma}_{12} \\ \overline{\sigma}_{13} \\ \overline{\sigma}_{23} \end{bmatrix} = \begin{bmatrix} \overline{E}_{1111} & \overline{E}_{1122} & \overline{E}_{1133} & \overline{E}_{1112} & \overline{E}_{1113} & \overline{E}_{1123} \\ \overline{E}_{2211} & \overline{E}_{2222} & \overline{E}_{2233} & \overline{E}_{2212} & \overline{E}_{2213} & \overline{E}_{2223} \\ \overline{E}_{3311} & \overline{E}_{3322} & \overline{E}_{3333} & \overline{E}_{3312} & \overline{E}_{3313} & \overline{E}_{3323} \\ \overline{E}_{1211} & \overline{E}_{1222} & \overline{E}_{1233} & \overline{E}_{1212} & \overline{E}_{1213} & \overline{E}_{1223} \\ \overline{E}_{1311} & \overline{E}_{1322} & \overline{E}_{1333} & \overline{E}_{1312} & \overline{E}_{1313} & \overline{E}_{1323} \\ \overline{E}_{2311} & \overline{E}_{2322} & \overline{E}_{2333} & \overline{E}_{2312} & \overline{E}_{2313} & \overline{E}_{2323} \end{bmatrix} \begin{bmatrix} \overline{\varepsilon}_{11} \\ \overline{\varepsilon}_{22} \\ \overline{\varepsilon}_{33} \\ 2\overline{\varepsilon}_{12} = \overline{\gamma}_{12} \\ 2\overline{\varepsilon}_{13} = \overline{\gamma}_{13} \\ 2\overline{\varepsilon}_{23} = \overline{\gamma}_{23} \end{bmatrix} \tag{4.3}$$

By defining the strain according to (4.4), it is possible to ensure that strain only occurs in one component. If the stated strain is implemented into (4.3), it becomes clear that only the first column of $\overline{\mathbf{E}}$ can be decided, which will be scaled depending on the magnitude of the applied strain according to (4.5). In a similar matter, this can be done for all virtual testing cases. The final result would then give the full homogenized elastic stiffness tensor, $\overline{\mathbf{E}}$. After the stiffness tensor has been defined, it is possible (for an isotropic volume element) to identify the elasticity modulus, E and the shear modulus, G or Poisson's ratio, ν. This is done according to Appendix A.

$$\begin{bmatrix} \overline{\varepsilon}_{11} \\ \overline{\varepsilon}_{22} \\ \overline{\varepsilon}_{33} \\ \overline{\gamma}_{12} \\ \overline{\gamma}_{13} \\ \overline{\gamma}_{23} \end{bmatrix} = \begin{bmatrix} \overline{\varepsilon}_{11} \\ 0 \\ 0 \\ 0 \\ 0 \\ 0 \end{bmatrix} \tag{4.4}$$

$$\begin{bmatrix} \overline{\sigma}_{11} \\ \overline{\sigma}_{22} \\ \overline{\sigma}_{33} \\ \overline{\sigma}_{12} \\ \overline{\sigma}_{13} \\ \overline{\sigma}_{23} \end{bmatrix} = \begin{bmatrix} \overline{E}_{1111} \\ \overline{E}_{1122} \\ \overline{E}_{1133} \\ \overline{E}_{1112} \\ \overline{E}_{1113} \\ \overline{E}_{1123} \end{bmatrix} \overline{\varepsilon}_{11} \tag{4.5}$$

It should be noted that this procedure will only be presented for equiaxed grains without texture as mentioned in chapter 1.2. In chapter 2.2, it is mentioned that equiaxed grains without texture give a homogenized isotropic material behavior. Therefore, the elastic stiffness tensor, $\overline{\mathbf{E}}$, should resemble the isotropic stiffness tensor, $\mathbf{D}$ (Ottosen & Petersson, 1992), here shown in Voigt form.

$$\mathbf{D} = \frac{E}{(1+\nu)(1-2\nu)} \begin{bmatrix} 1-\nu & \nu & \nu & 0 & 0 & 0 \\ \nu & 1-\nu & \nu & 0 & 0 & 0 \\ \nu & \nu & 1-\nu & 0 & 0 & 0 \\ 0 & 0 & 0 & \frac{1}{2}(1-2\nu) & 0 & 0 \\ 0 & 0 & 0 & 0 & \frac{1}{2}(1-2\nu) & 0 \\ 0 & 0 & 0 & 0 & 0 & \frac{1}{2}(1-2\nu) \end{bmatrix} \tag{4.6}$$

For plasticity, the homogenized result for the RVE is evaluated differently. Similarly to the elastic analysis, equations (4.1) and (4.2) are used to calculate the stresses and the strains for different virtual testing cases. However, several time-steps are required to solve the non-linear analysis. Therefore, the stresses and strains have to be homogenized for all time-steps. Thereafter, the result is gathered in stress-strain diagrams for the different load cases.

4.4.2 Individual grains

When analyzing the average behavior of the individual grains, the stresses and strains are calculated through a grain volume average, similarly to the procedure in chapter 4.4.1. However, the difference is

that each grain is examined separately. All the grains have different number of elements with a certain volume, therefore the stress calculation is done in accordance with (4.7). Once again, it should be noted that the calculations are done for simulations with virtual testing. After the stresses have been calculated for all grains, the stress distribution is plotted to get a visualization of how the stresses vary for the grains in the RVE. The strains can be calculated and plotted in a similar matter (4.8).

$$\overline{\boldsymbol{\sigma}}_{grain} = \frac{1}{V_{grain}} \sum_{e=1}^{n_{elem}} V_{e.grain}\, \boldsymbol{\sigma}_{e.grain} \tag{4.7}$$

$$\overline{\boldsymbol{\varepsilon}}_{grain} = \frac{1}{V_{grain}} \sum_{e=1}^{n_{elem}} V_{e.grain}\, \boldsymbol{\varepsilon}_{e.grain} \tag{4.8}$$

For the plastic analysis, the procedure is extended to include texture analyses of each element in each grain. As previously mentioned, the individual grains have a specific orientation described by Euler angles. When the specimen is loaded and deformed, the crystal orientations change. In CPFEM, each grain consists of several elements, which prior to deformation have the same crystal orientations. When loading is applied, each element is deformed individually. Therefore, it is necessary to evaluate the new slip directions for all the elements in the RVE after loading, which is done through B.11. To get the elastic deformation gradient, $\mathbf{F}^e$, SDV data related to $\mathbf{F}$ and $\mathbf{F}^p$ is extracted from the user subroutine, UMAT, in ABAQUS. From there, $\mathbf{F}^e$ can be calculated by utilizing equation (B.1). Thereafter, the new slip directions can be illustrated with pole figures by using standard MATLAB commands. It is also possible to calculate the new Euler-Bunge angles with equations (B.10)-(B.12). Afterwards, the new Euler angles can be used for plotting texture development in MTEX, which is an open-source MATLAB software that specifically focuses on illustrating crystallographic textures. However, in this report, the texture will be presented by own MATLAB pole plots of the slip directions.

4.5 J-AMEN

J-AMEN is an in-house code created by Dr. Jim Brouzoulis, which applies an elastic-plastic self-consistent (EPSC) based homogenization technique. It assumes that all grains are shaped in an ellipsoidal shape which is then surrounded by a homogeneous medium of infinite size (Li, Larsson, et al., 2021). The instantaneous stiffness tensor ($\mathrm{d}\bar{\boldsymbol{\sigma}}/\mathrm{d}\bar{\boldsymbol{\epsilon}}$) of this medium is the volume average of the instantaneous stiffness of all grains. Since EPSC modelling does not include interaction of the grains or inhomogeneous behavior within grains as in CPFEM, the method is more approximate. However, self-consistent based codes such as J-AMEN, require considerably less computational time compared to CPFEM simulations.

For equiaxed grains, the ellipsoid shapes can instead be represented with spheres. Similarly to CPFEM, an RVE can be used to represent all the grains. As a simplification, a 2-dimensional surface of the RVE can be seen in figure 4.5a. Here, each square in the grid represents a grain and its crystal orientation, marked in grey, with its surrounding medium, in white. By examining a 3-dimensional representation of one of the squares in figure 4.5b, it is possible to view the spherical representation of the grain surrounded by its infinite homogeneous matter. Material properties and crystal orientations needs to be defined for all the grains, similarly to what is done in CPFEM. In J-AMEN, loading can then be applied on each grain representation with regards to virtual testing and the results are almost instantly obtained. Since the material model and the load is defined in J-AMEN, it is not necessary to provide user defined codes such as UMAT and DISP. Additionally, J-AMEN does not require the meshed RVE from Neper. Therefore, only the crystal plasticity properties, Euler-Bunge angles and the defined loading are needed as input to the code.

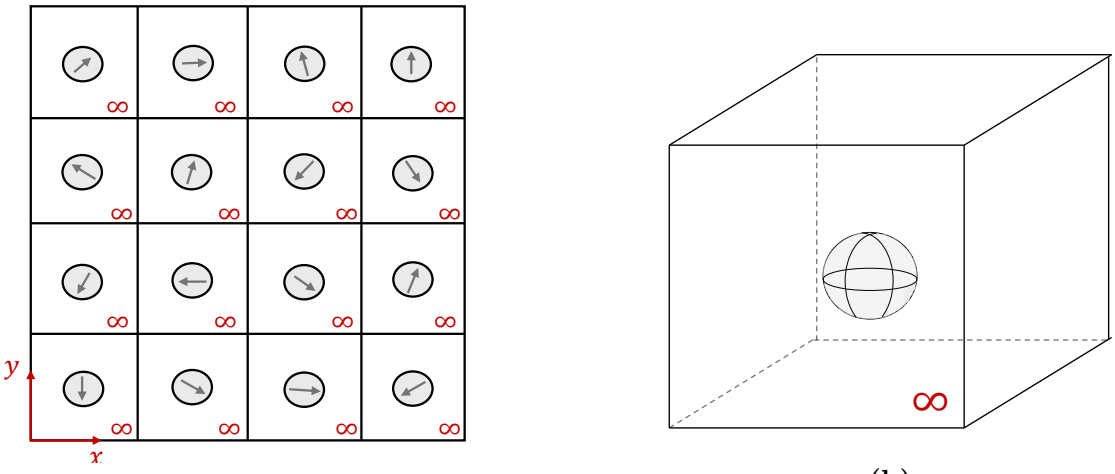

(a) (b)

Figure 4.5: *Simplified illustration of the RVE assumption for EPSC based modelling. A 2D illustration of the RVE can be seen in (a), with a 3D presentation of a single grain representation in (b).*

5 Elastic behavior of equiaxed grains in tension and shear

For the elastic analysis, results are extracted for equiaxed grains with material properties for Alloy 718. The first step is to conduct a mesh convergence study for the CPFEM analysis. Thereafter, an additional convergence study regarding the number of grains that are necessary to get an accurate homogenized stress-strain behavior is conducted for CPFEM. Then, the homogenized stress-strain behavior of the RVE is presented and compared to J-AMEN. Additionally, the individual grains' stress-strain response is studied and compared between CPFEM and J-AMEN.

5.1 Mesh convergence study

For the mesh convergence study, it is decided to analyze 500 equiaxed grains to ensure that the CPFEM analysis gives reasonable results. Three different mesh sizes are studied, where the coarsest mesh is created with rcl = 3, as seen in figure 5.1a. The coarsest mesh corresponds to 85891 elements. Thereafter, a finer mesh with rcl = 1 in figure 5.1b is analyzed, which results in 111442 elements. Additionally, a very fine mesh with 372295 elements is created by using rcl=0.5, as seen in 5.1c.

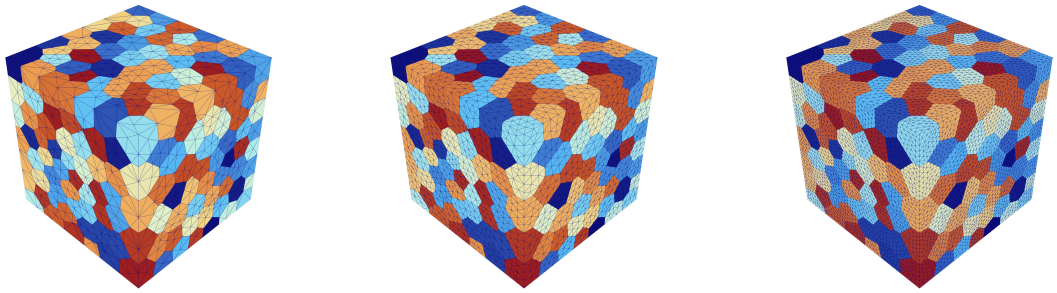

(a) **(b)** **(c)**

Figure 5.1: *Different meshes used for convergence study. (a) shows a coarse mesh with rcl = 3, (b) presents an intermediately fine mesh with rcl = 1, whilst (c) represents the fine mesh with rcl = 0.5.*

First, the material parameters are calculated and presented in table 5.1 for the different mesh sizes. It can be seen that the results already converge for the coarse mesh, as the difference between each material parameter is insignificant. This can also be noted by analyzing how the normal stress, $\overline{\sigma}_{11}$, in figure 5.2 and shear stress, $\overline{\sigma}_{12}$, in figure 5.3, vary over time. The homogenized stresses are plotted for each mesh size. In order to be able to clearly differentiate between the results when plotting, several time steps are used for the fine mesh even though the analysis is linear-elastic. Once again, there is not a big difference in results, therefore it is possible to use the coarsest mesh and still get accurate results. However, the difference in computational time between the coarse and medium mesh is not that big, therefore the medium sized mesh is used for the rest of the report as it gives slightly better results.

Table 5.1: *Convergence analysis of calculated material parameters for 500 grains*

Convergence study of material parameters : 500 grains			
Mesh	Coarse (rcl = 3)	Medium (rcl = 1)	Fine (rcl = 0.5)
E [GPa]	213.7	213.4	212.7
ν [-]	0.327	0.327	0.328
G [GPa]	79.7	79.5	79.0

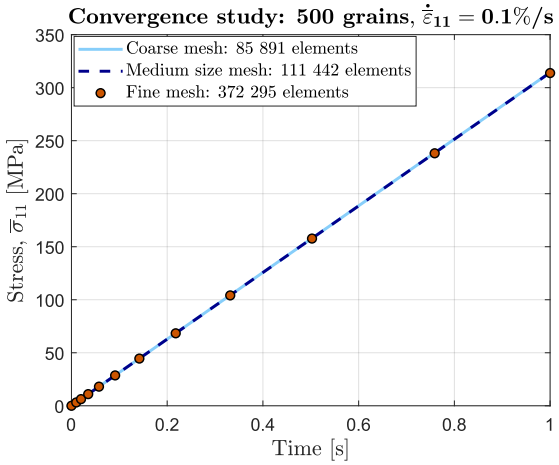

Figure 5.2: Convergence study on $\overline{\sigma}_{11}$, for 500 grains. Only $\overline{\varepsilon}_{11}$ is non-zero.

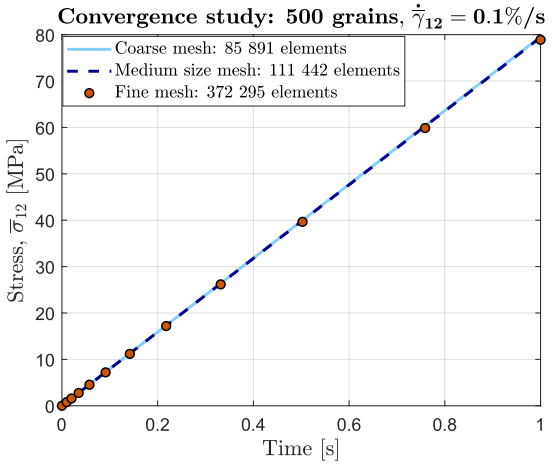

Figure 5.3: Convergence study on $\overline{\sigma}_{12}$, for 500 grains. Only $\overline{\gamma}_{12}$ is non-zero.

5.2 Homogenized stress-strain behaviour

In order to present valid results throughout the report, it is important to understand how many grains that are necessary to obtain a representative result of the microstructure. This is done for the homogenized stress-strain behavior in CPFEM, by comparing the calibrated values for Young's modulus, Poisson's ratio and the shear module. RVE's with 100-700 grains are created in Neper. The results are presented in table 5.2. It can be seen that the calibrated values for the material parameters match well for the different numbers of grains, however there is some discrepancy in results for 200 grains, which differs from the other grain structures. This could possibly be due to the randomized Bunge angles aligning more in a certain direction, hence the result for 200 grains. Regardless, a more consistent result can be for more than 300 grains. Therefore, to ensure accurate results while maintaining a reasonable computational time, it is decided that the analyses in the report will be made for 500 grains. The material parameters for CPFEM can then be compared to the result from J-AMEN in table 5.3. J-AMEN gives slightly lower values for Young's modulus and the shear modulus when comparing to CPFEM for 500 grains. Additionally, Poisson's ratio has a higher value than what is calibrated for CPFEM.

Table 5.2: *Calculated material parameters for equiaxed grain morphologies for FEM analysis*

Material parameters, CPFEM							
Grains	100	200	300	400	500	600	700
E [GPa]	212.7	209.4	212.5	214.6	213.4	213.5	212.4
ν [-]	0.328	0.330	0.328	0.326	0.327	0.327	0.328
G [GPa]	80.5	81.1	79.9	79.2	79.5	79.4	79.6

Table 5.3: *Calculated material parameters for equiaxed grain morpholgies for J-AMEN analysis of 500 grains.*

Material parameters, J-AMEN	
Grains	500
E [GPa]	199.2
ν **[-]**	0.339
G [GPa]	74.3

To get a better understanding of the differences in results for CPFEM and J-AMEN, the homogenized elastic stiffness tensor can be compared for the two methods. The result for CPFEM is presented in (5.1), while the elastic stiffness tensor for J-AMEN is shown in (5.2). By comparing the two matrices, there are some differences to note, especially for the values in the diagonal. For CPFEM, these values are slightly higher than what can be noted in J-AMEN. However, the results are still closely correlated, and since J-AMEN is a more approximate method than CPFEM a difference is expected. In addition, the calculated stiffness matrices closely resemble the isotropic stiffness matrix in equation (4.6), although it is more apparent for CPFEM. Even though full isotropy can not be viewed, the results still show that equiaxed grains have an overwhelmingly isotropic tendency. For a larger number of grains, this material behavior could very likely be more induced.

$$\overline{\mathbf{E}}_{500.\text{CPFEM}} = \begin{bmatrix} 314.18 & 152.07 & 151.35 & -0.044 & 0.0018 & 0.014 \\ 152.07 & 312.14 & 153.39 & -0.032 & -0.079 & -0.00047 \\ 151.35 & 153.39 & 312.86 & 0.076 & 0.077 & -0.013 \\ -0.022 & -0.016 & 0.038 & 78.40 & -2.039 & 0.77 \\ 0.00092 & -0.039 & 0.038 & -2.039 & 78.78 & -0.48 \\ 0.0069 & -0.00023 & -0.0066 & 0.77 & -0.48 & 80.41 \end{bmatrix} \text{[GPa]} \tag{5.1}$$

$$\overline{\mathbf{E}}_{500.\text{J-AMEN}} = \begin{bmatrix} 306.17 & 156.05 & 155.28 & -1.138 & -2.41 & 0.80 \\ 156.05 & 304.16 & 157.29 & 0.72 & 0.42 & -0.58 \\ 155.28 & 157.29 & 304.93 & 0.42 & 2.00 & -0.25 \\ 0.74 & -0.63 & -0.32 & 74.15 & -1.13 & 0.41 \\ -2.41 & 0.42 & 1.99 & -1.13 & 73.43 & -0.22 \\ -1.14 & 0.72 & 0.42 & 0.41 & -0.22 & 75.37 \end{bmatrix} \text{[GPa]} \tag{5.2}$$

5.3 Stress-strain behaviour of grains

For the individual grains' stress-strain distribution, the grain stress probability is analysed for both J-AMEN and CPFEM. This is done for the load case where $\overline{\varepsilon}_{11}$ is prescribed and the remaining strain components are zero, as well as when $\overline{\gamma}_{12}$ is prescribed and the remaining strain components are zero. The homogenized stress is calculated for each grain and illustrated in a distribution plot which shows how the stresses vary for the grains in the RVE. In figure 5.4, the stresses are plotted for the case when only $\overline{\varepsilon}_{11}$=0.1% , where (a) is CPFEM and (b) is J-AMEN. Additionally, the mean stress of the grains is plotted in a red dotted line. To differentiate between the results, it is decided to illustrate the stress variation in blue, where J-AMEN is presented in a lighter blue than CPFEM. By comparing the results, it is clear that the stress distribution is similar, although CPFEM gives a somewhat higher averaged stress. The majority of the grains in the CPFEM analysis, experience a stress around 330 MPa. In J-AMEN, the stresses are marginally lower, with peaks around 315 MPa. A similar observation can be made for figure 5.5, where (a) is the CPFEM result and (b) is the J-AMEN result when only $\overline{\gamma}_{12}$=0.1% is prescribed. Once again, the stress variations for the two different methods are closely related, however most grains in CPFEM have slightly larger stresses, around 95 MPa, compared to

85 MPa in J-AMEN. Because of this, the mean stress in CPFEM is higher than the one obtained for J-AMEN. Additionally, from figures 5.4 and 5.5 it can be noticed that there is less variation in stress magnitudes between the grains for J-AMEN than for CPFEM.

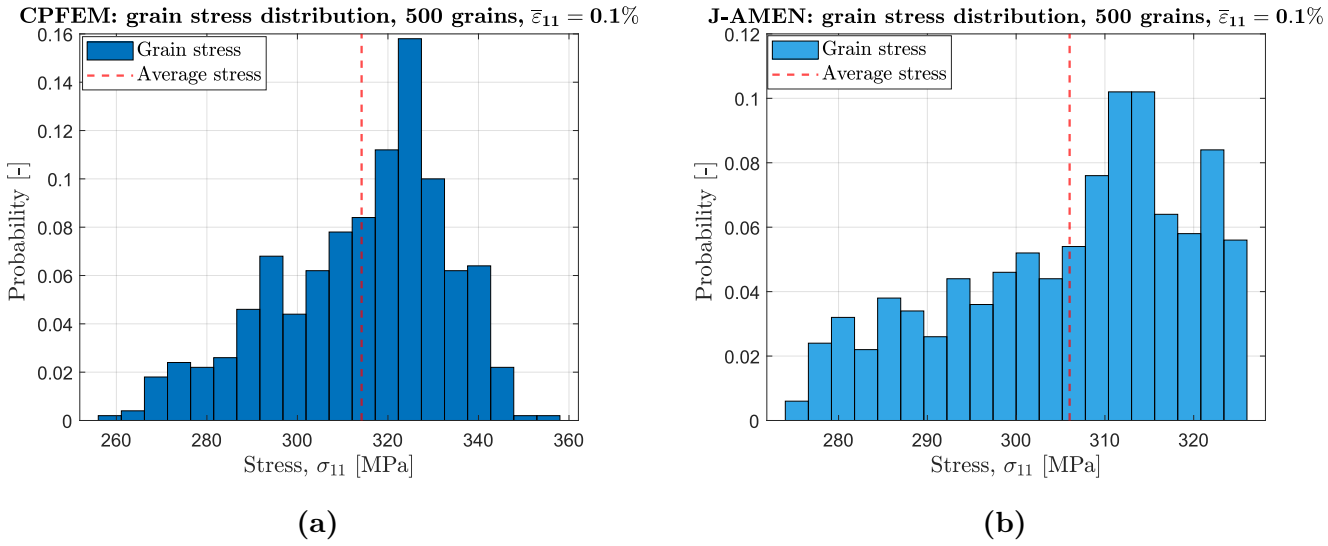

(a) **(b)**

Figure 5.4: *Average stress distribution for CPFEM (a) and J-AMEN (b), σ_{11}, for 500 grains. $\overline{\varepsilon}_{11}$ is controlled, while the other strain components are zero.*

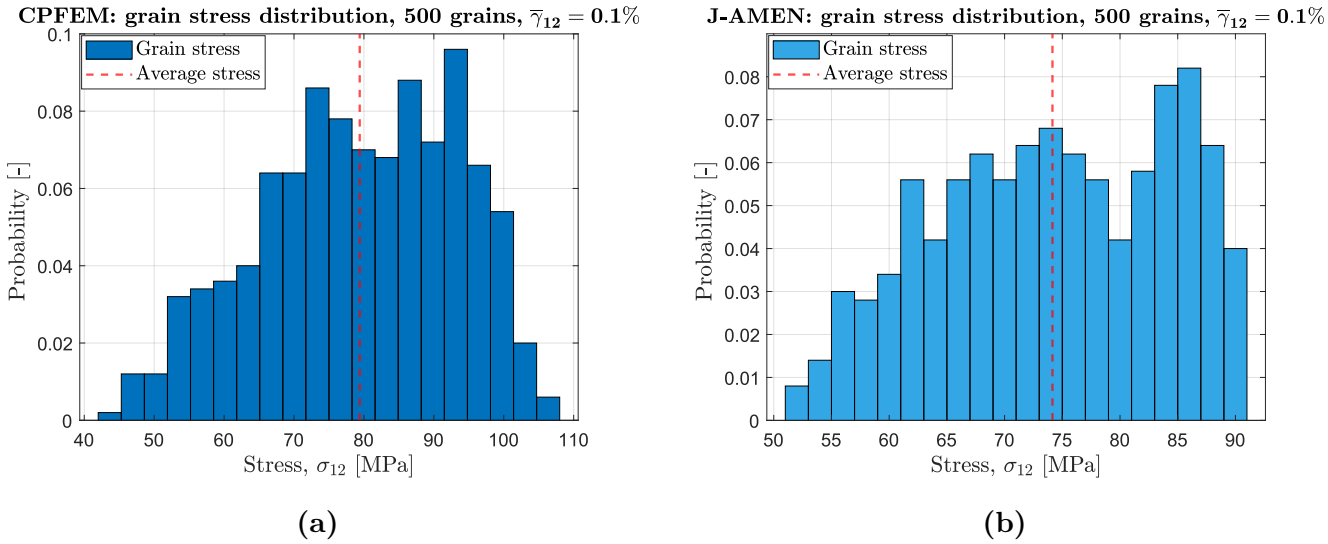

(a) **(b)**

Figure 5.5: *Average stress distribution for CPFEM (a) and J-AMEN (b), σ_{12}, for 500 grains. Only $\overline{\gamma}_{12}$ is controlled, while the other strain components are zero.*

The strain distribution for the grains is also investigated for the same load cases. Once again, to differentiate between the results, it is decided to illustrate the strain variation in green, where J-AMEN is plotted in a lighter green than CPFEM. By analyzing the grain strain distribution, it is possible to check if there is a correlation between the applied strain and the average, homogenized strain. To begin with, the load case where only $\overline{\varepsilon}_{11}$=0.1% applied is examined in figure 5.6 for CPFEM

(a) and J-AMEN (b). For CPFEM, it is possible to see that most grains experience a strain of 0.1%, while for J-AMEN the peak is slightly above 0.095%. However, the average strain for both routines is the same as the applied strain, which validates each method. In addition, the same analysis is made for the virtual testing case where $\overline{\gamma}_{12}$=0.1%. From figure 5.7a, it can be seen that most grains in the CPFEM analysis endure a strain around 0.1%, which also ends up being the average strain of the RVE. For J-AMEN, figure 5.7b depicts a slightly different strain distribution where several peaks occur around 0.09%, in addition to a peak at 0.1%. Similarly to the CPFEM results, the average strain in J-AMEN is around the same magnitude as the applied strain.

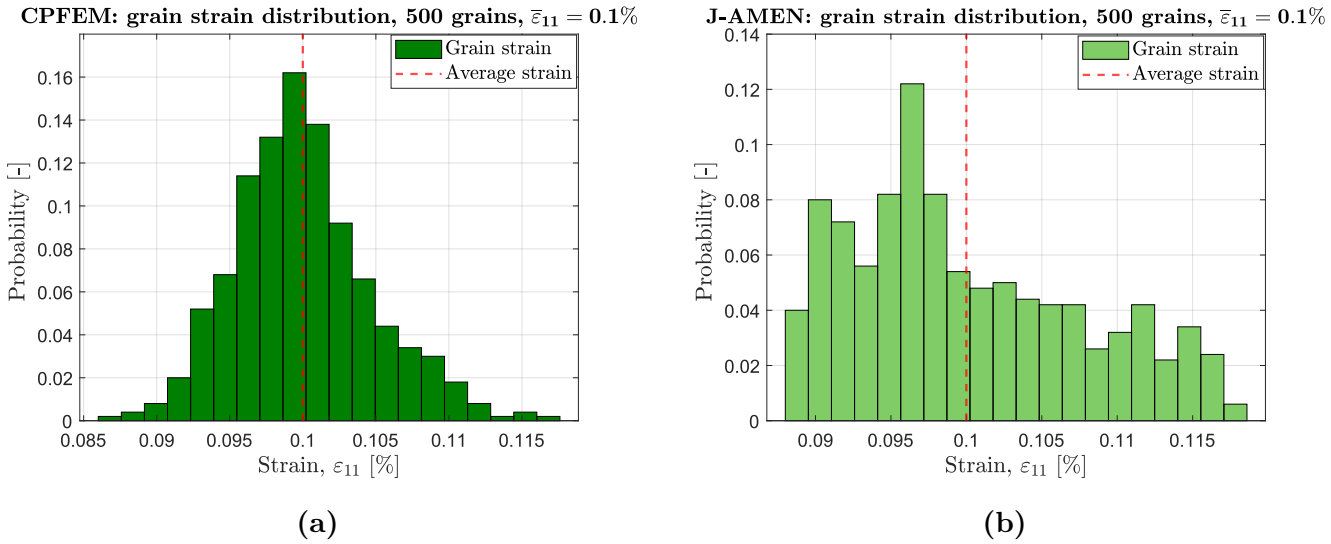

(a) **(b)**

Figure 5.6: *Average strain distribution for CPFEM (a) and J-AMEN (b), ε_{11}, for 500 grains. Only $\overline{\varepsilon}_{11}$ is controlled to a non-zero value (0.1%), while the other strain components are zero.*

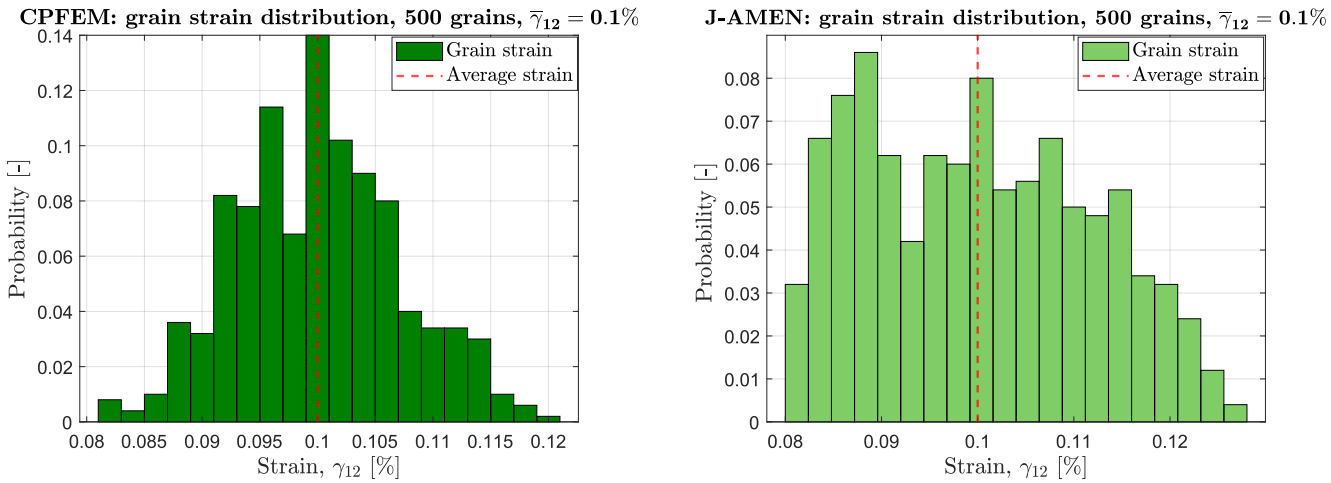

(a) **(b)**

Figure 5.7: *Average strain distribution for CPFEM (a) and J-AMEN (b), γ_{12}, for 500 grains. Only $\overline{\gamma}_{12}$ is controlled to a non-zero value (0.1%), while the other strain components are zero.*

6 Elasto-plastic behavior of equiaxed grains in shear

The plastic analysis for equiaxed grains is done for both Alloy 718 and Alloy 720Li. This is because it is of interest to investigate how J-AMEN approximates the stress-strain response for a 1-phase and 2-phase alloy, respectively. First, the number of grains necessary to give accurate results for a plastic analysis is investigated by comparing the stress-strain response for the homogenized CPFEM procedure. Thereafter, the homogenized stress-strain curves for CPFEM and J-AMEN are compared. The texture development after plasticity is analyzed for CPFEM only, since it was not possible to expand J-AMEN to include the texture analysis in the time span of this thesis.

6.1 Alloy 718

In this section, the results for Alloy 718 are presented. The analysis for the necessary number of grains is only conducted for this alloy. Additionally, the isotropic behavior of equiaxed grains is presented in this chapter.

6.1.1 Homogenized stress-strain behavior

In order to get an accurate depiction of how many grains that are necessary to get a good result for plasticity, the homogenized stress-strain behavior for CPFEM is analysed. In figure 6.1, the stress-strain curve for 100-700 grains is presented, for pure shear, where $\overline{\gamma}_{12} = 5\%$. Similarly to the elastic analysis in chapter 5.2, the result for 200 grains differs from the rest of the curves. The result for 100 grains and 300-700 grains, give closely correlated graphs, therefore 500 grains is once again chosen for the plastic analysis. Since the non-linear analysis requires several time steps, it is not as computationally demanding to run a model with less grains. It is possible to use a model with less than 500 grains and still get good results with a more reasonable computational time. However to keep consistency with the elastic analysis, 500 grains are chosen.

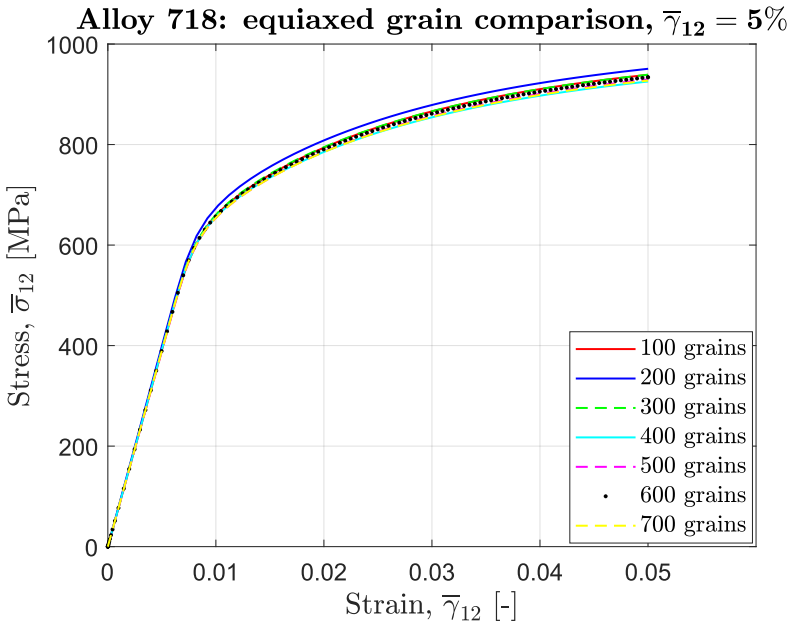

Figure 6.1: *Comparison of the number of equiaxed grains necessary to get an accurate result for plasticity. The results are gathered from CPFEM analysis. Pure shear is studied, where* $\overline{\gamma}_{12} = 5\%$.

Since it was concluded in chapter 5.1 that the medium sized mesh should be used for all models, an additional convergence study is not conducted for the plastic analysis. Therefore, it is possible to continue the study by comparing the homogenized stress-strain curve for 500 grains with CPFEM, for the different cases of pure shear. Here, pure shear analysis for $\overline{\gamma}_{12} = 5\%$, $\overline{\gamma}_{13} = 5\%$ and $\overline{\gamma}_{23} = 5\%$, is made separately and then compared in figure 6.2. It can be seen that the stress-strain for the different load cases are almost identical. This is due to the isotropy of equiaxed grains, which is still clear after plastic deformation. Because there is no deviation between the different load cases, only the pure shear case where $\overline{\gamma}_{12} = 5\%$ will be studied for the remaining parts of the report.

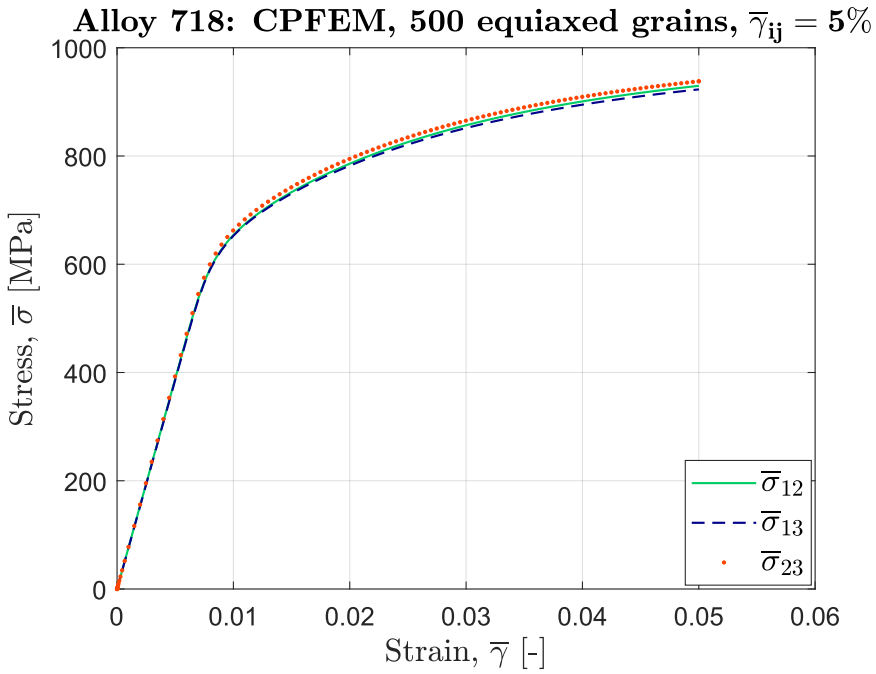

Figure 6.2: *Comparison of the stress-strain response for the different cases of pure shear. The analysis is done with CPFEM.*

A comparison between CPFEM and J-AMEN can now be made for 500 grains, for the pure shear load case, $\overline{\gamma}_{12} = 5\%$. From the result presented in figure 6.3, it is clear that the two different methods result almost identical stress-strain behaviour during loading. In the elastic region and at the beginning of the plastic response, J-AMEN approximates the material behavior exceptionally well to the CPFEM analysis. From 3% applied strain and further, the stress-strain curve for J-AMEN slightly deviates from the one obtained by CPFEM. However, the differences are small, which indicates that J-AMEN gives an accurate depiction of the material response for equiaxed grains under plastic loading. Since a convergence study on the number of grains is not conducted for J-AMEN, the stress-strain curve for 5000 grains with J-AMEN is plotted and compared to 500 grains in figure 6.3. There is a slight difference in results between J-AMEN for 500 and 5000 grains, although convergence has already occurred at 500 grains. However, the result for J-AMEN when analyzing 5000 grains is further away from the CPFEM results for 500 grains. This is unexpected, as one would assume that a larger number of grains would depict a more representative result when compared to the 500 grains in CPFEM that have already converged in terms of mesh and number of grains.

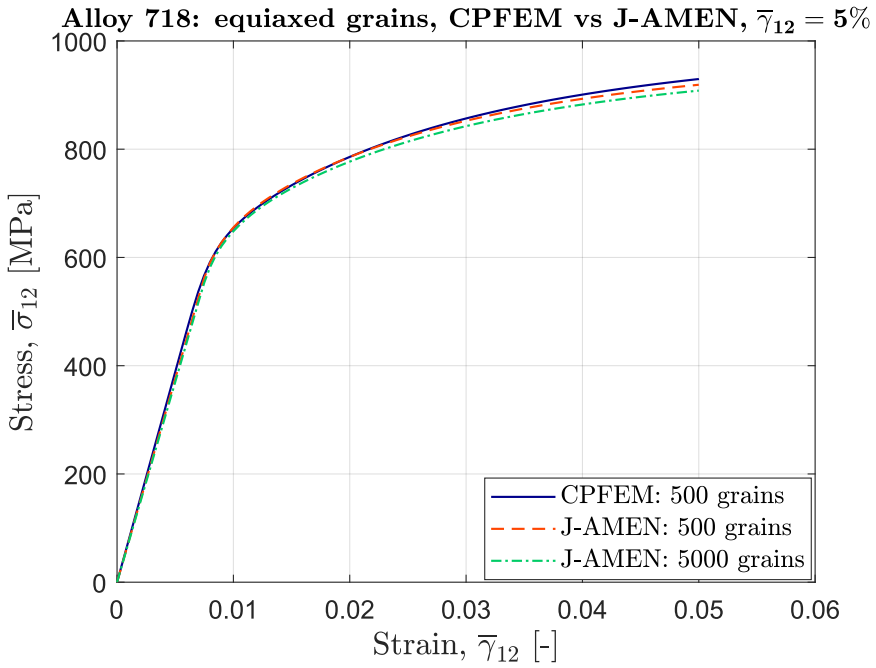

Figure 6.3: *Comparison of J-AMEN and CPFEM regarding the homogenized stress-strain behavior for Alloy 718. The analysis is made for 500 equiaxed grains loaded in pure shear, where $\overline{\gamma}_{12}$=5%.*

6.1.2 Texture development

The texture development is studied for all slip systems in table 3.1. For this analysis, the shear strain $\overline{\gamma}_{12}$ is incrementally increased to 20% and thereafter the slip directions for all slip systems, before and after deformation, can be calculated and illustrated in a pole figure. This is done for each element in the RVE for all slip systems. Therefore, the number of dots in each pole plot is the (number of elements for the entire RVE)*12. Figure 6.4a presents the pole figure prior to deformation. As seen, the dots are spread out, which is a sign of the random orientation of the grains. Two elements with a specific slip direction have been highlighted, one in red and the other in green. After 20% strain has been applied, a significant difference can be spotted in figure 6.4b. Since the deformation varies for each element, the crystal orientations change separately for all elements in the RVE. Therefore, the dots will move with regards to the deformation it experiences, which results in the dots spreading out over the studied *xy*-plane. This can be seen by analyzing how the red and green dots are moving after deformation. However, the slip direction for both of the highlighted elements does not change significantly. Therefore, it might be necessary to apply a higher shear strain to view a larger change in texture.

It should be noted that it looks as though there are more dots in figure 6.4b than in figure 6.4a. Before deformation occurs, all elements in a grain have the same crystal orientation and therefore the slip direction for each separate slip system is identical as well. This means that several dots in figure 6.4a have the same coordinates and are therefore plotted on top of each other, which gives the illusion that there are less dots before deformation. This applies for all pole figures presented in this report.

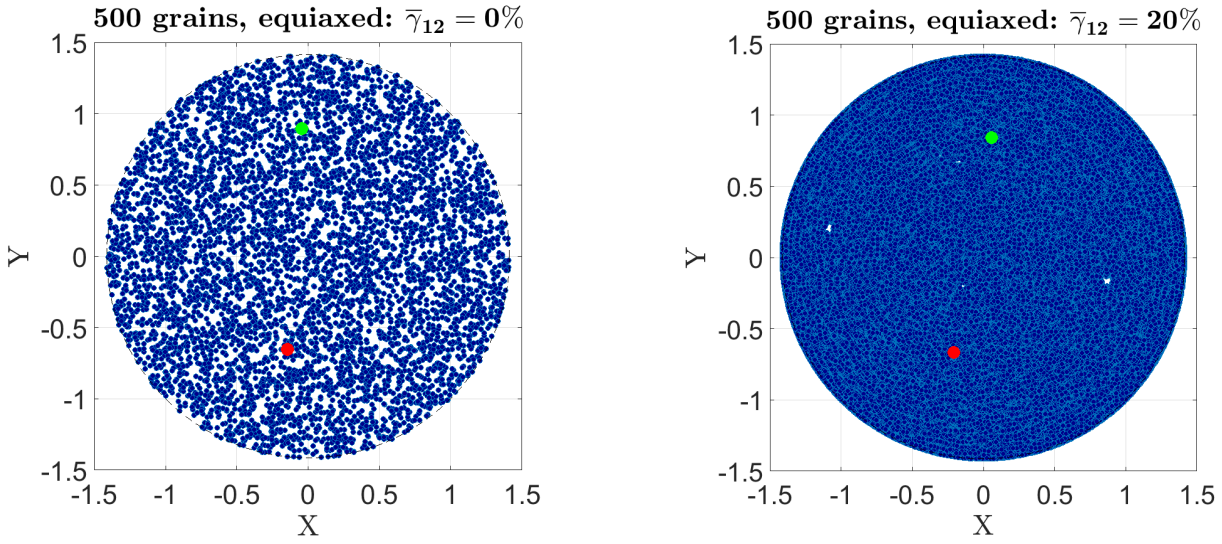

(a) **(b)**

Figure 6.4: *Texture development for 500 grains equiaxed grains with material properties corresponding to Alloy 718. The figure represent the texture before deformation (a) and after deformation, when $\overline{\gamma}_{12}$=20% (b). The texture development is studied for all twelve slip systems in table 3.1.*

6.2 Alloy 720Li

In chapter 6.1.1 it was decided that 500 grains were necessary to use for the plastic analysis, therefore this number of grains will also be studied for Alloy 720Li. Since the analysis for Alloy 720Li is also made for equiaxed grains, the load case of pure shear with $\overline{\gamma}_{12} = 5\%$ is used to compare CPFEM with J-AMEN, in accordance with what was concluded in chapter 6.1.1.

6.2.1 Homogenized stress-strain behavior

The stress-strain response of Alloy 720Li for CPFEM and J-AMEN is presented in figure 6.5. As for Alloy 718 in chapter 6.1.1, CPFEM and J-AMEN give similar results. For Alloy 720Li, the stress-strain response is almost identical, where the result slightly deviates between 1%-3% strain.

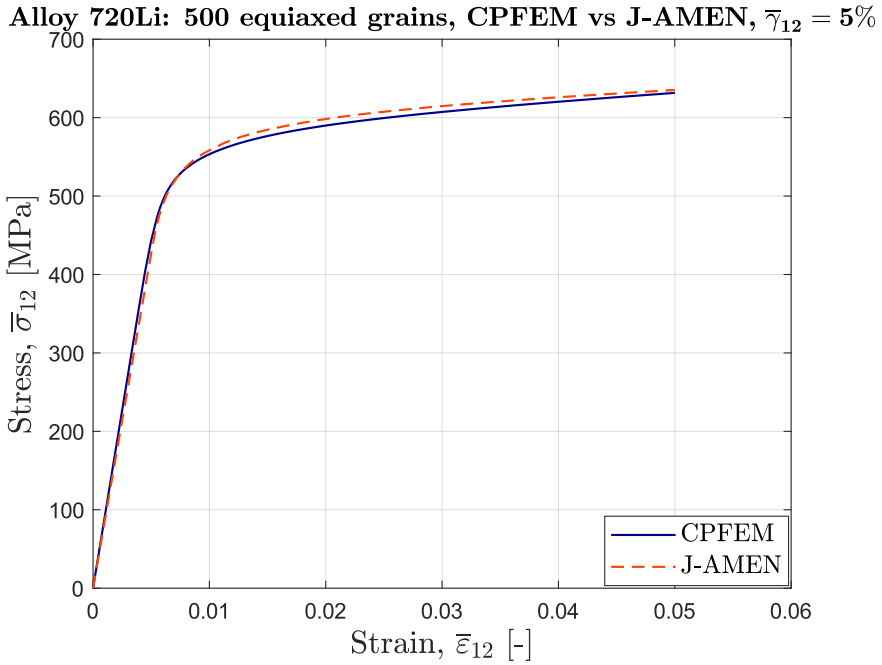

Figure 6.5: *Comparison of J-AMEN and CPFEM regarding the homogenized stress-strain behavior for Alloy 720Li. The analysis is made for 500 equiaxed grains loaded in pure shear, where* $\overline{\gamma}_{12}$*=5%.*

6.2.2 Texture development

Similarly to Alloy 718, the texture development during pure shear of $\overline{\gamma}_{12}$=20% for Alloy 720Li is in figure 6.6. Since the equiaxed grains have the same slip directions regardless of which alloy that is studied, figure 6.6a is identical to 6.4a where the same elements are highlighted once again. After deformation, it is from figure 6.6b clear that there is a big change in slip directions. However, the highlighted dots do not move significantly and the overall texture development is very similar to what was presented for Alloy 718 in figure 6.4b. Therefore, it can be concluded that a larger strain is necessary to apply for Alloy 720Li as well, in order to view a more prominent development in texture.

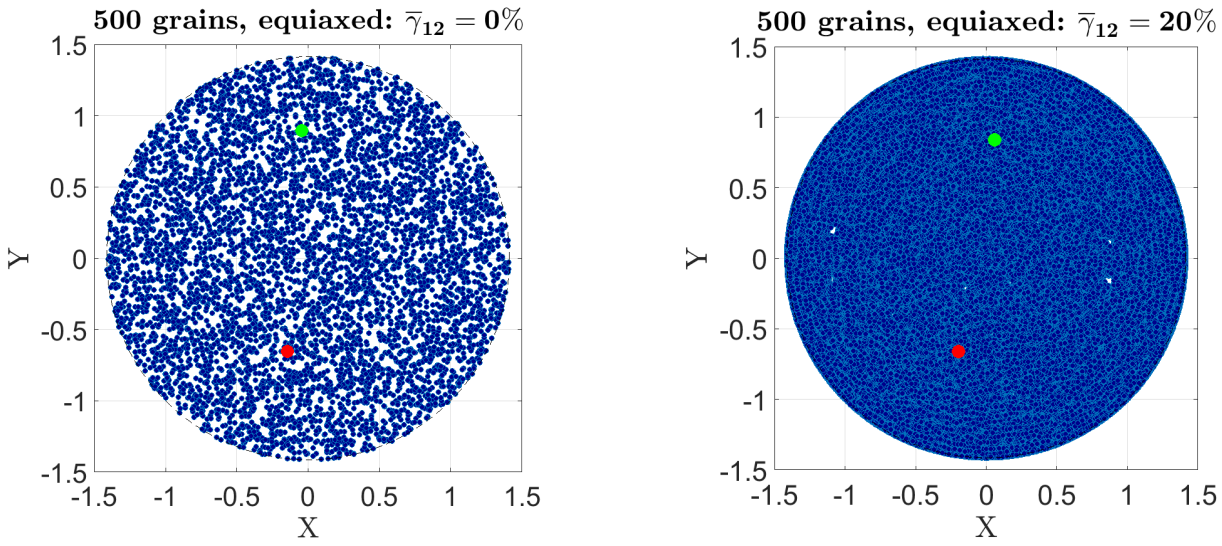

Figure 6.6: *Texture development for 500 grains equiaxed grains with material properties corresponding to Alloy 720Li. The figure represent the texture before deformation (a) and after deformation, when $\overline{\gamma}_{12}$=20% (b). The texture development is studied for all twelve slip systems in table 3.1*

7 Elasto-plastic behavior of elongated grains in shear

A plastic analyses of elongated grains are also presented in this report. However, J-AMEN does currently not include evaluation of elongated grains. Therefore, in this chapter, only CPFEM results will be presented, which can later be used to compare to J-AMEN after the code has been expanded to include elongated grains. The results will be presented for grains with an aspect ratio of 1:2 and 1:5 respectively, where the homogenized stress-strain behavior and texture development under loading will be examined. Additionally, a comparison between elongated grains with varying aspect ratios and equiaxed grains will be conducted for the CPFEM results. Since elongated grains are assumed to be transversely isotropic, the stress-strain response will vary depending on which loading direction that is examined. Therefore, loading in both the xy-direction and xz-direction are analyzed. The analyses are made for the medium mesh size presented in the convergence study, chapter 5.1.

7.1 Aspect ratio 1:2

Elongated grains with aspect ratio 1:2 are studied in this section, where the first step is to understand how many grains that are necessary to use get accurate results. Additionally, results of the homogenized stress-strain response for elongated grains under different cases of pure shear is presented. Thereafter, the texture development of the grains is analyzed.

7.1.1 Homogenized stress-strain behavior

First, 100-700 elongated grains with aspect ratio are analyzed for pure shear, $\overline{\gamma}_{12} = 5\%$, in the xy-direction, which can be seen in figure 7.1a. Similarly to the equiaxed grains in chapter 6.1.1, the result for 200 grains deviates from the other stress-strain curves. Once again, this could be due to the distribution of random orientations from Neper being more aligned towards a certain direction. However, the difference for elongated grains is that they are only oriented in their build direction, in this case the z-direction. Additionally, the discrepancy in the result could also be a sign that 200 grains are not sufficient enough to get a representative result. However, from 300 grains and upward, the stress-strain curves consistently match with minimal differences.

Similarly, by studying the response for pure shear, $\overline{\gamma}_{13} = 5\%$, in the xz-direction in figure 7.1b, it can be seen that the stress-strain curve for 200 grains still differs from the remaining ones. In addition, a representative stress-strain behavior is given after 300 grains. In order to preserve consistency with the elastic and plastic analysis for equiaxed grains, it is decided to use 500 grains for the remaining analyses for elongated grains with aspect ratio 1:2.

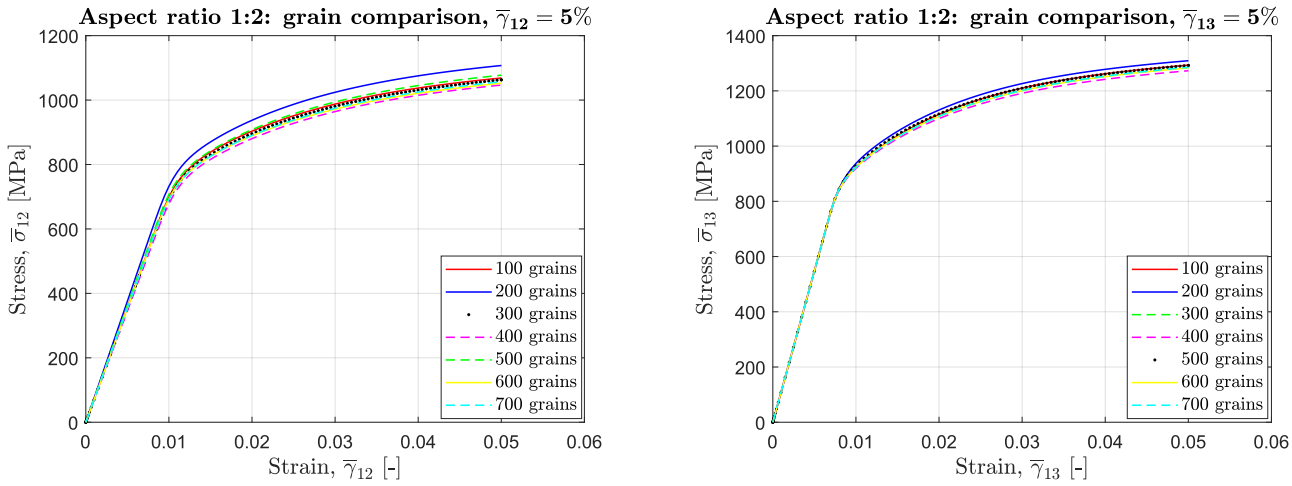

(a) **(b)**

Figure 7.1: *Comparison of the number of elongated grains with aspect ratio 1:2 that are necessary to get an accurate result for plasticity. The results are gathered from CPFEM analysis. Pure shear is studied, where (a) $\overline{\gamma}_{12} = 5\%$ and (b) $\overline{\gamma}_{13} = 5\%$.*

In order to understand the material behavior of elongated grains, the homogenized stress-strain curve for 500 grains for the different cases of pure shear is studied. The pure shear analysis is made for $\overline{\gamma}_{12} = 5\%$, $\overline{\gamma}_{13} = 5\%$ and $\overline{\gamma}_{23} = 5\%$ separately. In figure 7.2, the stress-strain curves from the different load cases are compared, and it can be noted that the material response is close to identical in the xz- and yz direction. The material response is expected, due to the grains being extracted in the z-direction, therefore it is enough to study the pure shear loading in the xz-direction. This can be explained with figure 2.3, by examining the xz-plane. Although not illustrated in the figure, the yz-plane is similar to the xz-plane, therefore the material response is almost the same for shearing in the different planes. From figure 7.2, it can also be noted that the material stiffness is lower for shearing along the xy-plane. This can also be visualized by inspecting figure 2.3. For clarity, it should be noted that figure 2.3 illustrates completely extruded columnar grains, while the analysis is made for elongated grains with a certain aspect ratio. However, the reasoning regarding the response during loading remains unchanged.

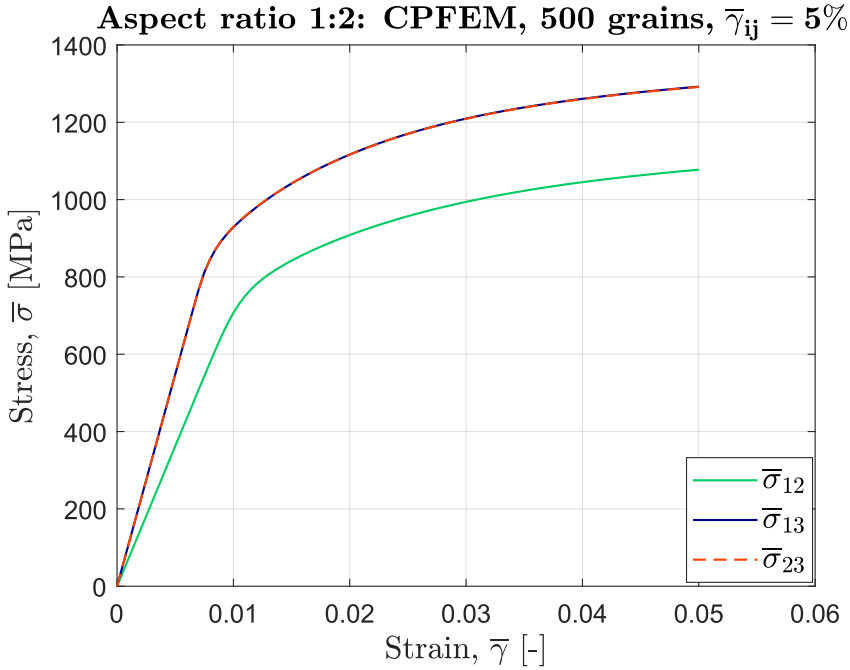

Figure 7.2: *Comparison of the stress-strain response for aspect ratio 1:2 for the different cases of pure shear. The analysis is done with CPFEM.*

7.1.2 Texture development

The texture development for the RVE containing elongated grains with aspect ratio is also studied. In order to capture the difference in the result due to anisotropy, two different load cases are examined: pure shear in the xy-direction and pure shear in the xz-direction. Figure 7.3 presents the pole figures before deformation (a) and after deformation (b), when $\overline{\gamma}_{12} = 20\%$.Prior to deformation, a clear pattern of dots in a circle can be seen. This is due to the elongated grains only having random orientation in the z-direction. When shearing is applied, the slip directions change, which is represented by the dots in figure 7.3b. The shearing in xy-direction becomes clear when viewing figure 7.3b, as the slip directions become skewed in that orientation.

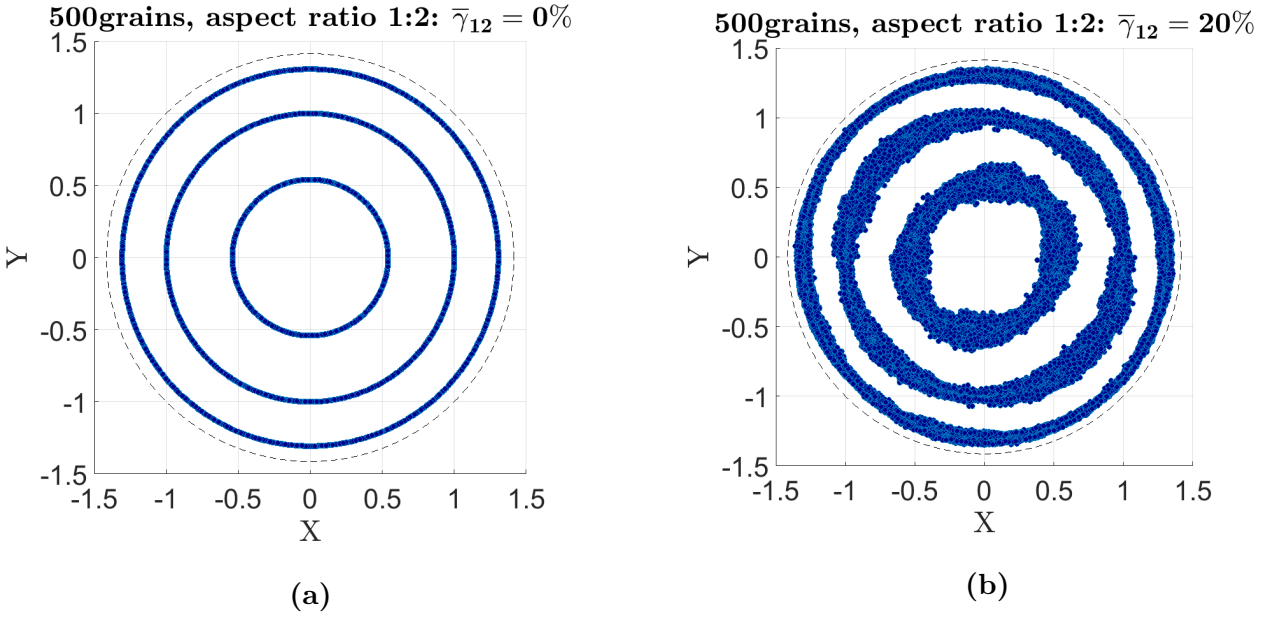

Figure 7.3: *Texture development for 500 grains with aspect ratio 1:2 and pure shear in the xy-direction. The figure represent the texture before deformation (a) and after deformation, when $\overline{\gamma}_{12}$=20% (b). The texture development is studied for all twelve slip systems in table 3.1*

The texture development for the load case where pure shear in the *xz*-direction is also studied, where $\overline{\gamma}_{13} = 20\%$. Once again, figure 7.4a presents the texture prior to deformation. Figure 7.4b shows how the texture changes after the applied shear load. Although the change in texture is not as visible as the pure shear load case where $\overline{\gamma}_{12} = 20\%$ in figure 7.3, it is definite that the texture changes after deformation.

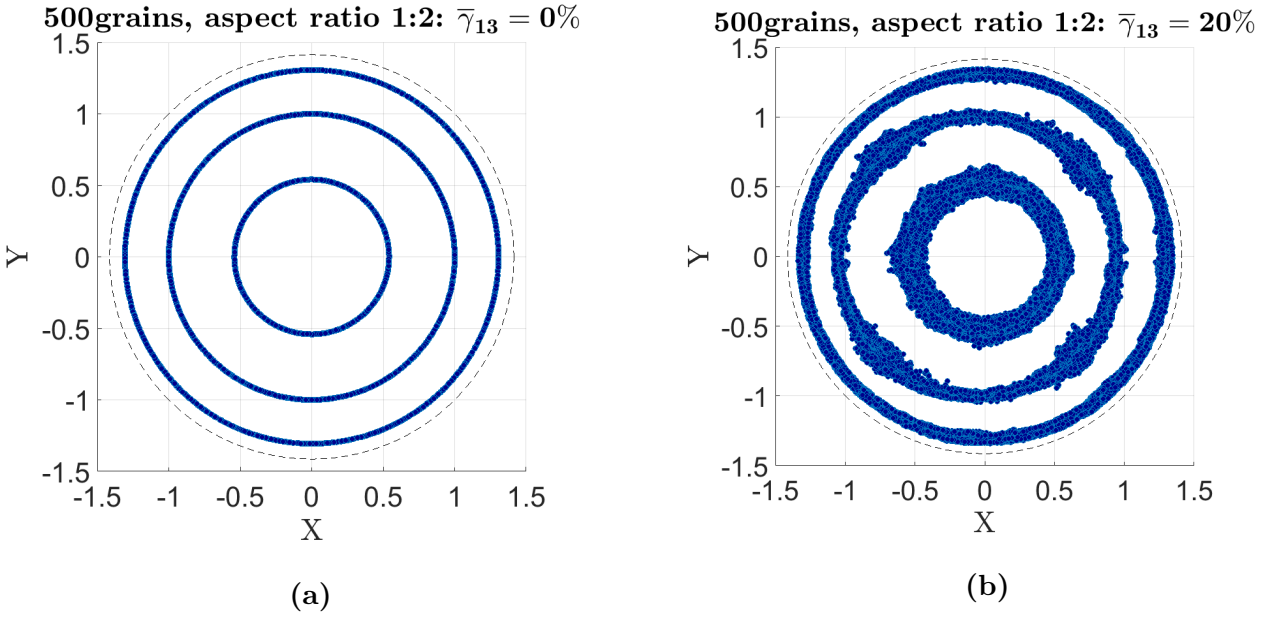

Figure 7.4: *Texture development for 500 grains with aspect ratio 1:2 and pure shear in the xy-direction. The figure represent the texture before deformation (a) and after deformation, when $\overline{\gamma}_{13}$=20% (b). The texture development is studied for all twelve slip systems in table 3.1*

7.2 Aspect ratio 1:5

Elongated grains with aspect ratio 1:5 are also studied for their material response during loading. This is done in the same manner as what was presented for elongated grains with aspect ratio 1:2 in chapter 7.1. It should be noted that although the shape of the grains for aspect ratio 1:5 is different to aspect ratio 1:2, they still have the same Euler-Bunge angles for each respective number of grains.

7.2.1 Homogenized stress-strain behavior

The first step is to analyze how many grains that are necessary to get a representative result. Similarly to before, 100-700 grains are studied, but this time with an aspect ratio of 1:5. Figure 7.5a presents the stress-strain diagrams for $\overline{\gamma}_{12} = 5\%$. By studying the result, it can be seen that for 100-300 grains, the results somewhat deviate from the other number of grains. For 400 grains and more, the stress-strain diagrams align in a more consistent matter. A similar, but not as noticeable, observation can be made in figure 7.5b, for the pure shear load case up to $\overline{\gamma}_{13} = 5\%$. Once again, the stress-strain diagrams start to show a consistent behavior from 400 grains and above. This result is in contrast to what was presented for equiaxed grains in chapter 6.1.1 and for elongated grains with aspect ratio 1:2 in chapter 7.1.1, where the stress-strain diagram for 200 grains was the only one that differed from the rest. From the results gathered for aspect ratio 1:5, it is decided to complete the remaining analyses with 500 grains to get a representable result.

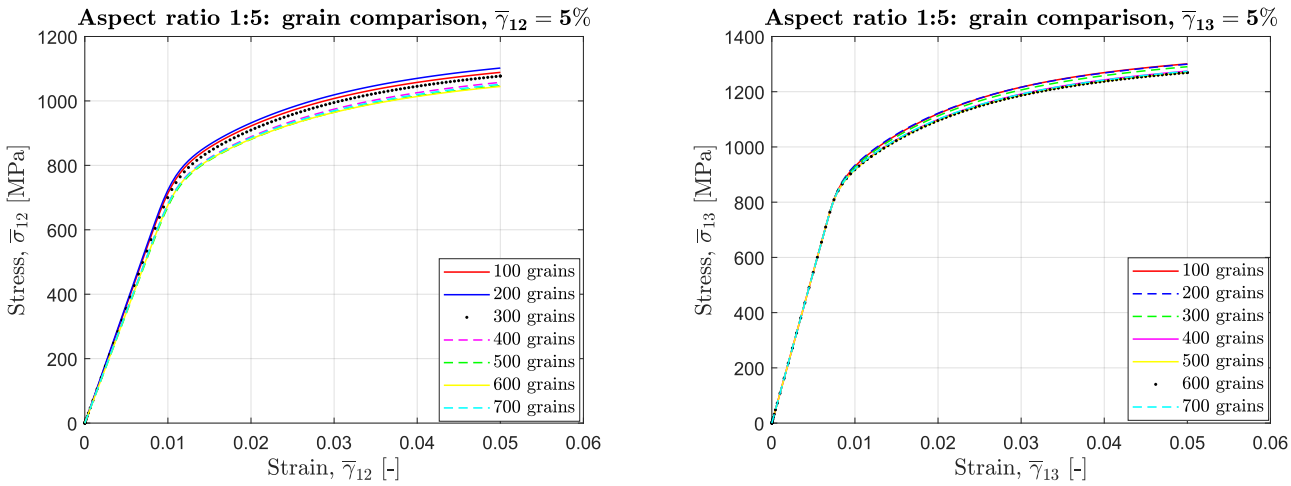

(a) **(b)**

Figure 7.5: *Comparison of the number of elongated grains with aspect ratio 1:5 that are necessary to get an accurate result for plasticity. The results are gathered from CPFEM analysis. Pure shear is studied, where (a) $\overline{\gamma}_{12}$=5% and (b) $\overline{\gamma}_{13}$=5%.*

Additionally, the stress-strain behavior is studied for the different cases of pure shear, where $\overline{\gamma}_{12}$=5%, $\overline{\gamma}_{13}$=5% and $\overline{\gamma}_{23}$=5% are analyzed separately and plotted in figure 7.6. Similarly to what was observed for elongated grains with aspect ratio 1:2 in figure 7.2, the material response for applied shear strain in the *xz*-direction and *yz*-direction are identical. In addition, the material stiffness is lower for shear in the *xy*-direction when compared to the other shear directions.

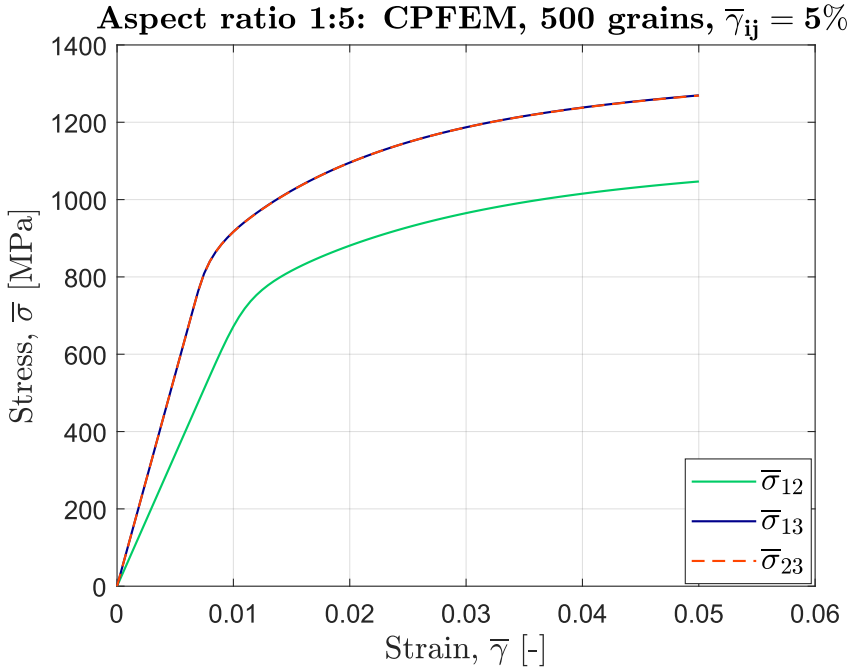

Figure 7.6: *Comparison of the stress-strain response for aspect ratio 1:5 for the different cases of pure shear. The analysis is done with CPFEM.*

7.2.2 Texture development

Similarly to the analysis in chapter 7.1.2, pure shear in the xy-direction and pure shear in the xz-direction, are examined for elongated grains, but now with an aspect ratio of 1:5. In figure 7.7, $\overline{\gamma}_{12} = 20\%$ is applied, where (a) presents the pole figures before deformation (b) presents the texture development after deformation. The result is very similar to what was presented in chapter 7.1.2 for pure shear in the xy-direction. Once again, the grains are only oriented in their build direction (z-direction), which gives the circular appearance in figure 7.7a. Additionally, the shearing of the slip direction is clearly visible in figure 7.7b.

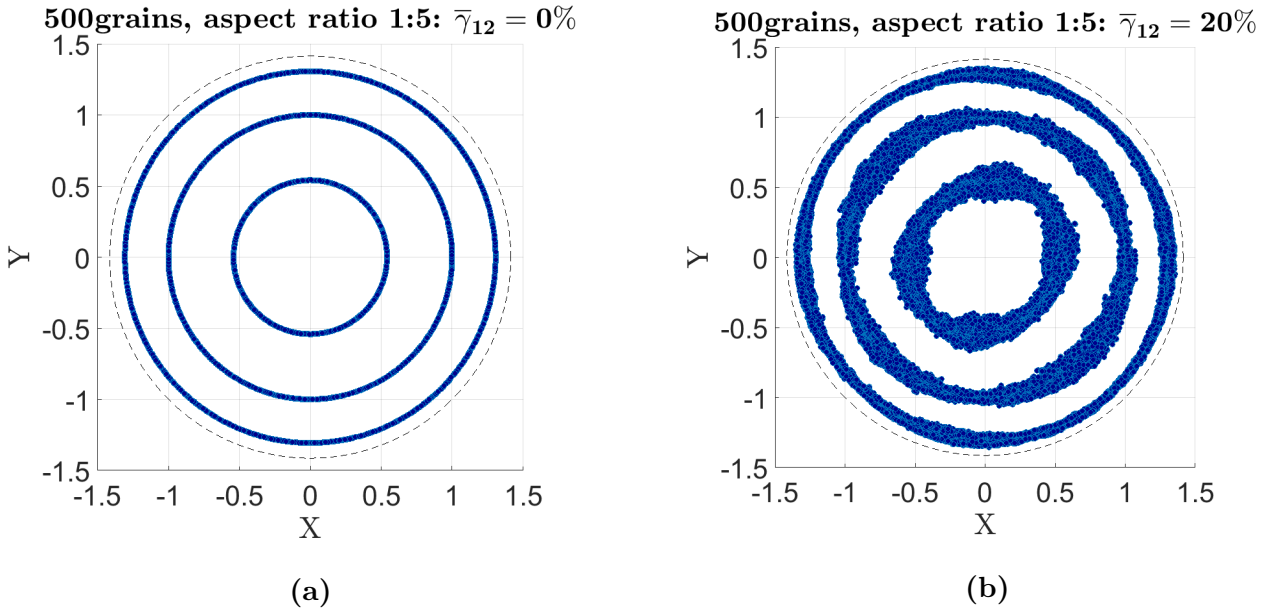

Figure 7.7: *Texture development for 500 grains with aspect ratio 1:5 and pure shear in the xy-direction. The figure represent the texture before deformation (a) and after deformation, when $\overline{\gamma}_{12}$=20% (b). The texture development is studied for all twelve slip systems in table 3.1*

In figure 7.8 the texture development is studied when $\overline{\gamma}_{13} = 20\%$ is applied, where (a) present the pole figure before deformation and (b) presents the texture development after deformation. Since the pole figure is not plotted in the same plane as the applied shear, it is more difficult to view the shearing of the slip directions. However, it is clear that there is a change in slip directions due to the external shear strain.

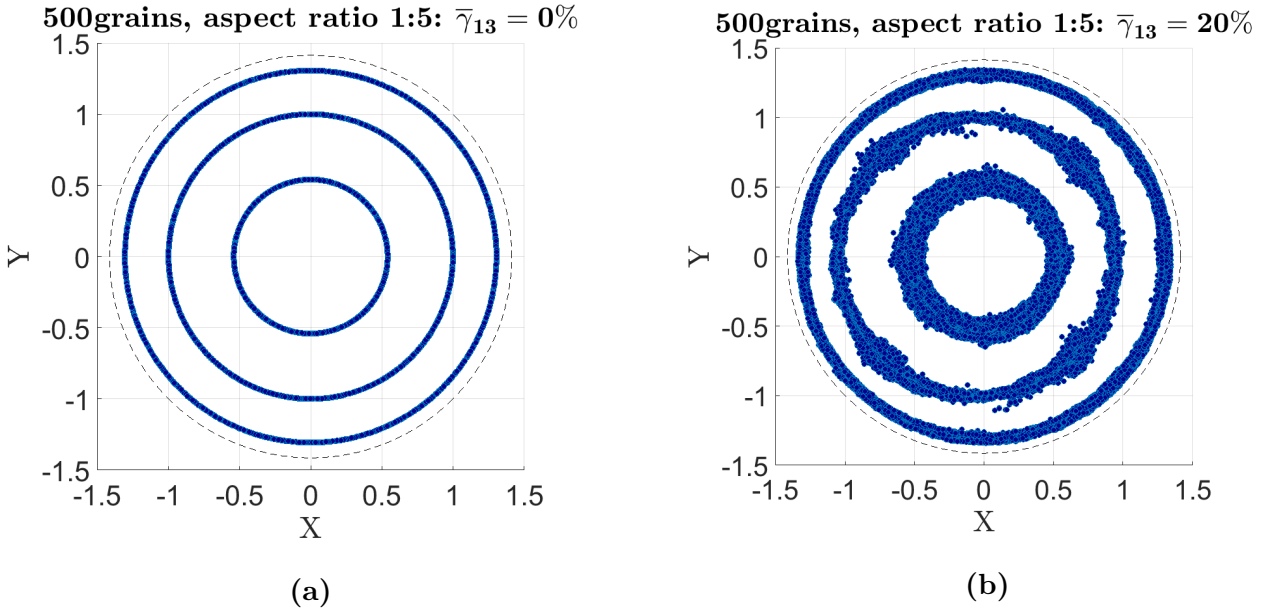

Figure 7.8: *Texture development for 500 grains with aspect ratio 1:5 and pure shear in the xz-direction. The figure represent the texture before deformation (a) and after deformation, when $\overline{\gamma}_{13}$=20% (b). The texture development is studied for all twelve slip systems in table 3.1*

7.3 Comparison: equiaxed versus elongated grains

To conclude the results regarding the material behavior during plastic loading for elongated and equiaxed grains, a comparison can be made for the different cases. In figure 7.9a and 7.9b, the load cases where only $\overline{\gamma}_{12}$ and $\overline{\gamma}_{13}$ are analyzed respectively for elongated grains with a aspect ratios from 1:2-1:10. This is done by comparing the stress-strain curves for 5% applied strain. Due to the response being similar for the different grain morphologies, it is from the figures difficult to differentiate the results. However, it is clear that there is not a big difference in the material response for the different aspect ratios.

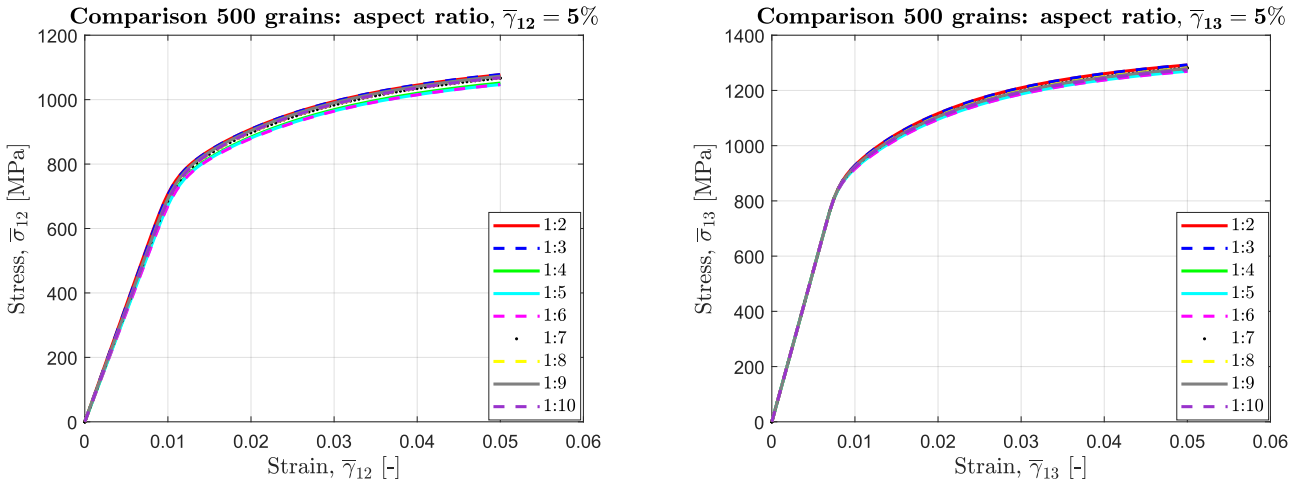

(a) **(b)**

Figure 7.9: *Comparison of 500 elongated grains with aspect ratios varying between 1:2-1:10. Pure shear is studied, where (a) $\overline{\gamma}_{12} = 5\%$ and (b) $\overline{\gamma}_{13} = 5\%$.*

It is also of interest to compare the stress-strain response for equiaxed grains versus elongated grains. This is made for 500 grains, where the studied aspect ratios are 1:2 and 1:5, respectively. First, the pure shear load case where $\overline{\gamma}_{12} = 5\%$ is analyzed and the results are presented in figure 7.10a. From the figure, it can be noted that the different grain morphologies behave similarly in the elastic region, but as plasticity starts to occur, differences can be seen between the curves. For instance, equiaxed grains exhibit lower stresses for the applied strain when compared to the elongated grains. Additionally, elongated grains with an aspect ratio of 1:2 present slightly higher stiffness than elongated grains with an aspect ratio of 1:5.

Secondly, in figure 7.10b, the results for the pure shear load case where $\overline{\gamma}_{13} = 5\%$ is presented. Since equiaxed grains have an isotropic material behavior, the stress-strain response is the same for loading in both *xy*-direction and *xz*-direction. However, since elongated grains exhibit an anisotropic material behavior during loading, the material stiffness behavior varies for the different shear directions. As seen in 7.10, a higher material stiffness can be seen in the *xz*-direction than in the *xy*-direction. Similarly to before, equiaxed grains have a lower stress-strain response during loading than elongated grains. Once again, elongated grains with an aspect ratio of 1:2 present slightly higher stiffness than elongated grains with an aspect ratio of 1:5.

Since grains with an aspect ratio of 1:2 have grains which are shaped closer to equiaxed grains, one would expect the stress-strain curve to be closer to the result for equiaxed grains. However, from the results it is seen that grains with an aspect ratio of 1:5 have a stress-strain curve which is closer

to the one for equiaxed grains. In addition, the difference in result between aspect ratio 1:2 and 1:5 is very small, which can also be noted for all aspect ratios presented in figure 7.9. This indicates that it is not the shape of the grains that decides the stress-strain behavior, instead it is the texture of the grains. There is a big difference in grain morphologies between aspect ratio 1:2 and 1:10, however, the stress-strain curves are almost identical, which is due to the strong texture where grains are only randomly oriented along the *z-direction*.

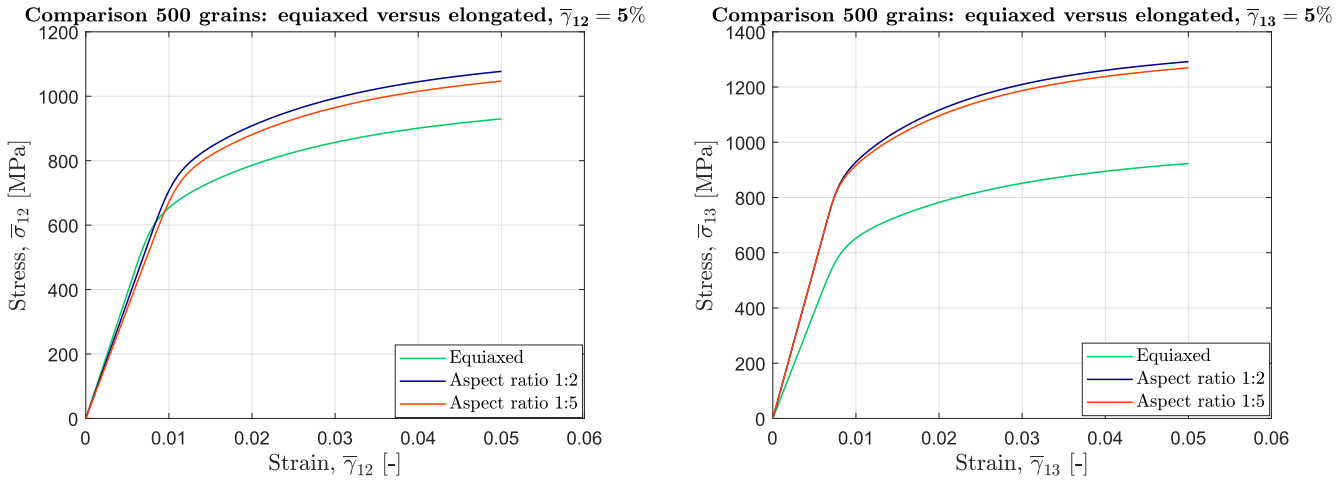

(a) **(b)**

Figure 7.10: *Comparison between equiaxed grains and elongated grains with an aspect ratio of 1:2 and 1:5, respectively. The analysis is made for 500 grains and pure shear is studied, where (a) $\overline{\gamma}_{12} = 5\%$ and (b) $\overline{\gamma}_{13} = 5\%$.*

Also, by comparing the texture development between aspect ratio 1:2 and 1:5, it is clear that there is barely any difference in the results. This can be seen when comparing figure 7.3 for aspect ratio 1:2 with figure 7.7 for aspect ratio 1:5, when all strain components are zero except for $\overline{\gamma}_{12}$. Once again, it should be noted that since the grain morphologies with elongated grains have the same slip directions before deformation, their respective pole figures for this stage are identical. However, even after deformation the difference in result is not noticeable between the different grain morphologies. The same reasoning can be applied for shear in the *xz*-direction, where figure 7.4 presents the pole figures for aspect ratio 1:2, while 7.8 presents the result for aspect ratio 1:5. In addition, the texture development for Alloy 718 (6.4) and Alloy 720Li (6.6) is almost identical. If a higher strain is applied for both alloys, it might be possible to differentiate between the results while also getting a more prominent texture development.

8 Concluding remarks and future work

The aim of this thesis was to compare J-AMEN to CPFEM in terms of to accuracy and computational time. Three main analyses were performed, where the first one focused on elasticity for equiaxed grains in pure tension and pure shear. The results showed that J-AMEN and CPFEM are in relatively good agreement. Therefore, J-AMEN produces accurate results for elasticity when compared to CPFEM. This applies for both the homogenized stress-strain behavior and the behavior for individual grains. However, in terms of computational time, there is not a big difference between J-AMEN and CPFEM as both methods run comparatively fast for the elastic analysis. Thus, it can be concluded that either J-AMEN or CPFEM can be used for an elastic analysis in multiscale modeling and still give accurate results for a short computational time.

However, it is the plastic analysis that is the most interesting to investigate as CPFEM then becomes computationally demanding. For the plastic analysis, the homogenized stress-strain behavior was investigated for equiaxed grains. Simulations for J-AMEN and CPFEM were performed for two different metals: Alloy 718 and Alloy 720Li. J-AMEN presents a very accurate stress-strain behavior for both metals when compared to CPFEM. Additionally, the computational time for J-AMEN is significantly less, as it only took 1-2 minutes to perform the analysis. In contrast, it took around two hours until the plastic analysis in CPFEM was completed for 500 grains up to 5% strain. Therefore, it would be preferable to use J-AMEN in multiscale modeling when analyzing plasticity, as it produced accurate results without demanding a lot of computational time.

It was also computationally expensive to run the simulations for elongated grains. Additionally, for RVE's with more than 500 grains, the FEM simulations took around 2 hours. The texture analyzes were made for 20% strain, which resulted in computational times between 2-4 hours, depending on the grain morphology and the alloy being studied. It should be mentioned that the CPFEM calculations were made on the cluster. If the simulations were run locally, it is expected that the computational time would be significantly longer. If one also considers the time for preparing the CPFEM analyses, such as creating and meshing the RVE and extracting the data, then the total time would be significantly higher.

For future work, it is clear that J-AMEN needs to be extended, such that it includes analyses of elongated grains and texture development. For now, the use of J-AMEN for multiscale modeling is limited to equiaxed grain, where the elastic analysis can be made to study the homogenized stress-strain behavior in addition to the response for each grain. However, as previously mentioned, it is the plastic analysis that is most interesting as it requires significant computational time for CPFEM. Although it has been proven that J-AMEN gives reasonable results compared to CPFEM for the homogenized elasto-plastic behavior in shear, it still needs to be expanded to include the texture development of grains during loading.

Since microstructures of metals sometimes consists of elongated grains, it is also important to include this microstructure into J-AMEN. From the presented results for elongated grains from CPFEM, it was shown that it is not the shape of the grains that plays a big role in the material behavior during loading, it is the texture. This information could be valuable for the extension of J-AMEN. A first step would be to apply the textured crystal orientations in J-AMEN with spherical grain representation and compare the homogenized stress-strain behavior to that from CPFEM. If the aspect ratio of the grains actually is low importance, then the results between the two methods should match relatively well.

In terms of microstructures analyzed, it would also be interesting to see how a mixed microstruc-

ture with both equiaxed and elongated grains would compare for J-AMEN and CPFEM. Of course, this would require a further extension of the J-AMEN code. If the mixed microstructure has random orientations for the grains, then it is not enough to have spherical representations of the grains in J-AMEN because the result would be identical to equiaxed grains. Therefore, a mixed microstructure would require information about the shape of the grains. Additionally, it is of interest to conduct the homogenization analyses for more grains than what was studied in this thesis to get a more representative result. However, due to the time constraint of the thesis, this was not investigated. In the future, it would also be valuable to compare CPFEM and J-AMEN by conducting a full multiscale modeling procedure.

References

ABAQUS. (2006). *Abaqus - version 6.6 documentation*. https://classes.engineering.wustl.edu/2009/spring/mase5513/abaqus/docs/v6.6/index.html

Agius, D., Mamun, A. A., Truman, C., Mostafavi, M., & Knowles, D. (2022). A method to extract slip system dependent information for crystal plasticity models. *MethodsX*, *9*. https://doi.org/https://doi.org/10.1016/j.mex.2022.101763

Bhattacharyya, A., Kalidindi, S., Doherty, & Davidge, R. (2002). Investigating the evolution of grain scale microstructure during large plastic deformation of polycrystalline aluminum.

Bunge, H.-J. (1982). 2 - orientation of individual crystallites. In H.-J. Bunge (Ed.), *Texture analysis in materials science* (pp. 3–41). Butterworth-Heinemann. https://doi.org/https://doi.org/10.1016/B978-0-408-10642-9.50007-6

Chen, H., Meng, C., & Liu, Y. (2022). Modeling elasticity of cubic crystals using a novel nonlocal lattice particle method. *Computational Mechanics*, *69*(5). https://search.ebscohost.com/login.aspx?direct=true&db=edsgao&AN=edsgcl.701029523&site=eds-live&scope=site&authtype=guest&custid=s3911979&groupid=main&profile=eds

Daymond, M., Preuss, M., & Clausen, B. (2007). Evidence of variation in slip mode in a polycrystalline nickel-base superalloy with change in temperature from neutron diffraction strain measurements. *Acta Materialia*, *55*(9). https://doi.org/https://doi.org/10.1016/j.actamat.2007.01.013

Dequiedt, J. (2018). The incidence of slip system interactions on the deformation of fcc single crystals: System selection and segregation for local and non-local constitutive behavior. *International Journal of Solids and Structures*, *141-142*, 1–14. https://doi.org/https://doi.org/10.1016/j.ijsolstr.2018.01.008

Dreelan, D., Ivankovic, A., & Browne, D. J. (2023). Grain structure predictions for metallic additive manufacturing processes. *IOP Conference Series: Materials Science and Engineering*, *1274*(1), 1–7. https://doi.org/10.1088/1757-899X/1274/1/012013

Eshragi, M., & Yoshioka, J. (2023). Temporal evolution of temperature gradient and solidification rate in laser powder bed fusion additive manufacturing. *Heat and Mass Transfer*, *59*, 1155–1166. https://doi.org/https://doi.org/10.1007/s00231-022-03318-8

Flowers, P., William R. Robinson, P., Langley, R., & Theopold, K. (2015). Chemistry. OpenStax. https://openstax.org/books/chemistry/pages/10-6-lattice-structures-in-crystalline-solids

Geers, M. G. D., Kouznetsova, V. G., Matouš, K., & Yvonnet, J. (2017). Homogenization methods and multiscale modeling: Nonlinear problems. In *Encyclopedia of computational mechanics second edition* (pp. 1–34). John Wiley & Sons, Ltd. https://doi.org/https://doi.org/10.1002/9781119176817.ecm2107

Greer, A. L. (2016). Overview: Application of heterogeneous nucleation in grain-refining of metals. *The Journal of Chemical Physics*, *145*(21), 211–704. https://doi.org/10.1063/1.4968846

Gundgire, T., Goel, S., Klement, U., & Joshi, S. (2020). Response of different electron beam melting produced alloy 718 microstructures to thermal post-treatments. *Materials Characterization*, *167*. https://doi.org/https://doi.org/10.1016/j.matchar.2020.110498

Hagenlocher, C., O'Toole, P., Xu, W., Brandt, M., Easton, M., & Molotnikov, A. (2022). In process monitoring of the thermal profile during solidification in laser directed energy deposition of aluminium. *Additive Manufacturing Letters*, *3*. https://doi.org/https://doi.org/10.1016/j.addlet.2022.100084

Kelly, A., & Knowles, K. M. (2020). *Crystallography and crystal defects (3rd edition)*. John Wiley & Sons. https://app.knovel.com/kn/resources/kpCCDE0006/toc?cid=kpCCDE0006

Kok, Y., Tan, X., Wang, P., Nai, M., Loh, N., Liu, E., & Tor, S. (2018). Anisotropy and heterogeneity of microstructure and mechanical properties in metal additive manufacturing: A critical review. *Materials & Design*, *139*, 565–586. https://doi.org/https://doi.org/10.1016/j.matdes.2017.11.021

Kumara, C., Deng, D., Moverare, J., & Nylén, P. (2018). Modelling of anisotropic elastic properties in alloy 718 built by electron beam melting. *Materials Science and Technology*, *34*(5), 529–537. https://doi.org/10.1080/02670836.2018.1426258

Li, H., Huang, Y., Jiang, S., Lu, Y., Gao, X., Lu, X., Ning, Z., & Sun, J. (2021). Columnar to equiaxed transition in additively manufactured cocrfemnni high entropy alloy. *Materials and Design*, *197*, 109–262. https://doi.org/https://doi.org/10.1016/j.matdes.2020.109262

Li, H., Larsson, F., Colliander, M. H., & Ekh, M. (2021). Elastic-viscoplastic self-consistent modeling for finite deformation of polycrystalline materials. *Materials Science and Engineering: A*, *799*. https://doi.org/https://doi.org/10.1016/j.msea.2020.140325

March, N. G., Gunasegaram, D. R., & Murphy, A. B. (2023). Evaluation of computational homogenization methods for the prediction of mechanical properties of additively manufactured metal parts. *Additive Manufacturing*, *64*, 103–415. https://doi.org/https://doi.org/10.1016/j.addma.2023.103415

Mouritz, A. P. (2012). In *Introduction to aerospace materials* (pp. 57–90). Woodhead Publishing. https://doi.org/https://doi.org/10.1533/9780857095152.57

Narayana Samy, V. P., Schäfle, M., Brasche, F., Krupp, U., & Haase, C. (2023). Understanding the mechanism of columnar–to-equiaxed transition and grain refinement in additively manufactured steel during laser powder bed fusion. *Additive Manufacturing*, *73*, 103–702. https://doi.org/https://doi.org/10.1016/j.addma.2023.103702

Ottosen, N. S., & Petersson, H. (1992). *Introduction to the finite element method*. Prentice Hall.

Quey, R., & Kasemer, M. (2022). The neper/fepx project: Free / open-source polycrystal generation, deformation simulation, and post-processing. *IOP Conference Series: Materials Science and Engineering*, *1249*(1), 1–9. https://doi.org/10.1088/1757-899X/1249/1/012021

Segurado, J., & Llorca, J. (2013). Simulation of the deformation of polycrystalline nanostructured ti by computational homogenization [Selected Publications of the EU FP7 project VIRTUAL NANOTITANIUM (VINAT)"Theoretical analysis and virtual testing of titanium-based nanomaterials"]. *Computational Materials Science*, *76*. https://doi.org/https://doi.org/10.1016/j.commatsci.2013.03.008

Sun, S., Zhang, X., Cui, J., & Liang, S. (2020). Identification of the miller indices of a crystallographic plane: A tutorial and a comprehensive review on fundamental theory, universal methods based on different case studies and matters needing attention. *Nanoscale*, (12). https://doi.org/10.1039/D0NR03637D

Todaro, C. J., Easton, M., Qiu, D., Zhang, D., Bermingham, M., Lui, E. W., Brandt, M., StJohn, D. H., & Qian, M. (2020). Grain structure control during metal 3d printing by high-intensity ultrasound. *Nature communications*, *11*(1). https://doi.org/https://doi.org/10.1038/s41467-019-13874-z

Tomé, C. N., & Lebensohn, R. A. (2023). 1 - basic concepts. In C. N. Tomé & R. A. Lebensohn (Eds.), *Material modeling with the visco-plastic self-consistent (vpsc) approach*. Elsevier. https://doi.org/https://doi.org/10.1016/B978-0-12-820713-0.00001-1

Wei, H., Lyu, D., Hu, W., & Wu, C. T. (2022). Rve analysis in ls-dyna for high-fidelity multiscale material modeling, 1–11. https://doi.org/https://doi.org/10.48550/arXiv.2210.11761

Yang, G., & Park, S.-J. (2003). Deformation of single crystals, polycrystalline materials, and thin films: A review. *Materials (Basel, Switzerland), 12*(12). https://doi.org/10.3390/ma12122003

Zaikovska, L., Ekh, M., & Kumara, C. (2023). Virtual testing of synthetic polycrystal microstructures predicting elastic properties of additive manufactured alloy 718. *Proceedings of the 9th World Congress on Mechanical, Chemical, and Material Engineering (MCM'23)*. https://doi.org/https://doi.org/10.11159/icmie23.147

Zhang, Y., Hu, Z., & Guo, L. (2021). Study on a new forming method—thread rolling by crystal plasticity finite element simulation. *Metals*, *11*. https://doi.org/10.3390/met11030503

Zhong, C., Kittel, J., Gasser, A., & Schleifenbaum, J. H. (2019). Study of nickel-based super-alloys inconel 718 and inconel 625 in high-deposition-rate laser metal deposition. *Optics & Laser Technology*, *109*, 352–360. https://doi.org/https://doi.org/10.1016/j.optlastec.2018.08.003

A Calibration of E, G and ν

It should be noted that this calibration procedure strictly applies for the equiaxed grains, as they present an isotropic material behavior. Columnar grains are transversely isotropic, therefore an average value of E, G and ν can not be calculated. Instead, one would end up with a separate values for each direction.

The homogenized elastic stiffness tensor is defined in (A.1).

$$\overline{\mathbf{E}} = \begin{bmatrix} \overline{E}_{1111} & \overline{E}_{1122} & \overline{E}_{1133} & \overline{E}_{1112} & \overline{E}_{1113} & \overline{E}_{1123} \\ \overline{E}_{2211} & \overline{E}_{2222} & \overline{E}_{2233} & \overline{E}_{2212} & \overline{E}_{2213} & \overline{E}_{2223} \\ \overline{E}_{3311} & \overline{E}_{3322} & \overline{E}_{3333} & \overline{E}_{3312} & \overline{E}_{3313} & \overline{E}_{3323} \\ \overline{E}_{1211} & \overline{E}_{1222} & \overline{E}_{1233} & \overline{E}_{1212} & \overline{E}_{1213} & \overline{E}_{1223} \\ \overline{E}_{1311} & \overline{E}_{1322} & \overline{E}_{1333} & \overline{E}_{1312} & \overline{E}_{1313} & \overline{E}_{1323} \\ \overline{E}_{2311} & \overline{E}_{2322} & \overline{E}_{2333} & \overline{E}_{2312} & \overline{E}_{2313} & \overline{E}_{2323} \end{bmatrix} \tag{A.1}$$

For an isotropic material, $\overline{\mathbf{E}}$, should correspond to the $\mathbf{D}$-matrix defined in (A.2).

$$\mathbf{D} = \frac{E}{(1+\nu)(1-2\nu)} \begin{bmatrix} 1-\nu & \nu & \nu & 0 & 0 & 0 \\ \nu & 1-\nu & \nu & 0 & 0 & 0 \\ \nu & \nu & 1-\nu & 0 & 0 & 0 \\ 0 & 0 & 0 & \frac{1}{2}(1-2\nu) & 0 & 0 \\ 0 & 0 & 0 & 0 & \frac{1}{2}(1-2\nu) & 0 \\ 0 & 0 & 0 & 0 & 0 & \frac{1}{2}(1-2\nu) \end{bmatrix} \tag{A.2}$$

In order to extract the elastic material parameters, it is necessary to take the inverse of the stiffness matrix. If one does this for the $\mathbf{D}$-matrix in expression (A.2), the result is $\mathbf{D}^{-1}$ (A.3).

$$\mathbf{D}^{-1} = \frac{1}{E} \begin{bmatrix} 1 & -\nu & -\nu & 0 & 0 & 0 \\ -\nu & 1 & -\nu & 0 & 0 & 0 \\ -\nu & -\nu & 1 & 0 & 0 & 0 \\ 0 & 0 & 0 & 2(1+\nu) & 0 & 0 \\ 0 & 0 & 0 & 0 & 2(1+\nu) & 0 \\ 0 & 0 & 0 & 0 & 0 & 2(1+\nu) \end{bmatrix} \tag{A.3}$$

Since $\overline{\mathbf{E}}$ corresponds to $\mathbf{D}$, $\overline{\mathbf{E}}^{-1}$ will correspond to $\mathbf{D}^{-1}$. Therefore, after the stiffness tensor $\overline{\mathbf{E}}$ has been defined, it is possible to calibrate the elasticity modulus, E, the shear modulus, G and Poisson's ratio, ν. In order to calculate E, it can from equation(A.3) be seen that the first three diagonal values give the elastic modulus in each normal direction. Therefore, this can be calculated for the homogenized stiffness tensor $\overline{\mathbf{E}}$ (A.4).

$$E_{11} = \frac{1}{\overline{\mathbf{E}}^{-1}(1,1)}, \quad E_{22} = \frac{1}{\overline{\mathbf{E}}^{-1}(2,2)}, \quad E_{33} = \frac{1}{\overline{\mathbf{E}}^{-1}(3,3)} \tag{A.4}$$

Generally, the shear modulus G, can be calculated according to (A.5). From expression (A.3), the last three diagonals represent the inverse if this expression. Therefore, G can be calculated in all shear directions according to (A.6).

$$G = \frac{E}{2(1+\nu)} \tag{A.5}$$

$$G_{12} = \frac{1}{\overline{\mathbf{E}}^{-1}(4,4)}, \quad G_{13} = \frac{1}{\overline{\mathbf{E}}^{-1}(5,5)}, \quad G_{23} = \frac{1}{\overline{\mathbf{E}}^{-1}(6,6)} \tag{A.6}$$

Since equiaxed grains are fully isotropic, the elastic modulus should almost be the same in each normal direction. The same reasoning is applied for the shear modulus. Therefore, the mean values of E and G can be calculated by taking the average value of the stiffness parameters for elasticity and shear (A.7).

$$E = \frac{E_{11} + E_{22} + E_{33}}{3}, \quad G = \frac{G_{12} + G_{13} + G_{23}}{3} \tag{A.7}$$

Similarly, by examining (A.3), Poisson's ratio can be calculated for all shear directions (A.8), (A.9), (A.10). Just as before, Poisson's ratio should not differ significantly for all shear directions and therefore a mean value can be calculated (A.11).

$$\nu_{12} = -\overline{E}^{-1}(2,1) \cdot E_{11}, \quad \nu_{21} = -\overline{E}^{-1}(1,2) \cdot E_{22} \tag{A.8}$$

$$\nu_{13} = -\overline{E}^{-1}(3,1) \cdot E_{11}, \quad \nu_{31} = -\overline{E}^{-1}(1,3) \cdot E_{33} \tag{A.9}$$

$$\nu_{23} = -\overline{E}^{-1}(3,2) \cdot E_{22}, \quad \nu_{32} = -\overline{E}^{-1}(2,3) \cdot E_{33} \tag{A.10}$$

$$\nu = \frac{\frac{\nu_{12}+\nu_{21}}{2} + \frac{\nu_{13}+\nu_{23}}{2} + \frac{\nu_{23}+\nu_{32}}{2}}{3} \tag{A.11}$$

To ensure that an isotropic Hooke's law is obtained, Poisson's ratio can alternatively, from equation (A.5), be computed as $\nu = E/(2\,G) - 1$

B Crystal plasticity model: large deformations

In this appendix, the crystal plasticity model is presented in terms of large deformations (Segurado & Llorca, 2013). To begin with, the model assumes that the deformation gradient can be described as a multiplicative split of the elastic and the plastic deformation gradients in accordance with (B.1).

$$\mathbf{F} = \mathbf{F}^e\mathbf{F}^p \tag{B.1}$$

By describing (B.1) in terms of the velocity gradient $\mathbf{L}$, the expression (B.2) is obtained, where (B.3) describes the plastic velocity gradient.

$$\mathbf{L} = \dot{\mathbf{F}}\mathbf{F}^{-1} = \dot{\mathbf{F}}^e\dot{\mathbf{F}}^{e^{-1}} + \mathbf{F}^e\dot{\mathbf{F}}^p\mathbf{F}^{p^{-1}}\mathbf{F}^{e^{-1}} \tag{B.2}$$

$$\mathbf{L}^p = \dot{\mathbf{F}}^p\mathbf{F}^{p^{-1}} \tag{B.3}$$

To describe that plastic deformation that occurs on multiple slip planes, the plastic velocity gradient can be calculated by summing the shear rates, $\dot{\gamma}^\alpha$, of each slip system α (B.4).

$$\mathbf{L}^p = \sum_{\alpha=1}^{n} \dot{\gamma}^\alpha \mathbf{s}_0^\alpha \otimes \mathbf{m}_0^\alpha \tag{B.4}$$

Since it is assumed that the crystals have an elasto-viscoplastic material response, the shear rate, can be described by (B.5), which is identical to what was presented for small deformations.

$$\dot{\gamma}^\alpha = \dot{\gamma}_0 \left(\frac{|\tau^\alpha|}{g^\alpha} \right)^{\frac{1}{m}} sign(\tau^\alpha) \tag{B.5}$$

The elastic strain (B.6) $\mathbf{E}^e$ is formulated as

$$\mathbf{E}^e = \frac{1}{2}\left(\mathbf{C}^e - \mathbf{I}\right) \tag{B.6}$$

where the elastic Cauchy-Green deformation tensor $\mathbf{C}^e$ is defined as

$$\mathbf{C}^e = \mathbf{F}^{e^T}\mathbf{F}^e \tag{B.7}$$

The second-order elastic Piola-Kirchhoff tensor, $\mathbf{S}^e$, describes the stress and is related to the elastic strain $\mathbf{E}^e$ by the fourth-order stiffness tensor of a single crystal, $\mathbb{C}$ (B.8).

$$\mathbf{S}^e = \mathbb{C} : \mathbf{E}^e \;\text{ or }\; S_{ij}^e = C_{ijkl}E_{kl}^e \tag{B.8}$$

The resolved shear stress (Schmid stress), τ^α (B.9), can in large deformation setting be expressed as

$$\tau^\alpha = \left(\mathbf{C}^e\,\mathbf{S}^e\right) : \left(\mathbf{s}_0^\alpha \otimes \mathbf{m}_0^\alpha\right) \tag{B.9}$$

on the system described by $\mathbf{s}_0^\alpha \otimes \mathbf{m}_0^\alpha$. The expressions and equations for the critical shear stress is the same as for the small deformation model described in chapter 3.5.

As illustrated in figure 3.5, each slip system can be described with the slip plane normal and slip direction in table 3.1. Since each grain has its own set of Euler angles, the rotated slip plane normal $\boldsymbol{m}_0^\alpha$ and slip direction $\boldsymbol{s}_0^\alpha$ can be described in accordance with (B.10) (Agius et al., 2022). In this expression, $\mathbf{R}$ describes the rotation matrix for the Euler angles before deformation, while $\boldsymbol{m}_{00}^\alpha$ and $\boldsymbol{s}_{00}^\alpha$ are the values from table 3.1 for a certain slip system. The slip system prior to deformation forms an orthonormal base vector by including $\boldsymbol{l}_{00}^\alpha = \boldsymbol{s}_{00}^\alpha \times \boldsymbol{m}_{00}^\alpha$. When the specimen is loaded, the crystal orientations change (Bhattacharyya et al., 2002). The elastic deformation gradient, $\mathbf{F}^e$, relates to

both the orientation transformation and the elastic deformations. The change in crystal orientation due to plasticity is insignificant, therefore $\mathbf{F}^p$ only defines the shearing between slip systems. Because of this, the transformation of the slip plane normal and slip direction can be described by (B.11). Here the inverse transpose of $\mathbf{F}^e$ is used for the slip plane normal, $\boldsymbol{m}_\alpha$, to ensure that the slip direction and slip plane remain orthogonal to each other before and after deformation.

Additionally, to obtain a unique solution of the Euler-Bunge angles after deformation, the slip system, $\boldsymbol{l}_\alpha$, needs to be used (B.11). Then, it is possible to solve the system of equations to get the Euler angles after loading (B.12). Here, $\mathbf{R}_t$ is the only unknown variable, and contains the crystal orientations after deformation, which are to be solved with the equation system. Thereafter, the crystal orientations and their variation during loading can be described with pole figures (Bhattacharyya et al., 2002).

$$\mathbf{m}_0^\alpha = \mathbf{R}\mathbf{m}_{00}^\alpha, \quad \mathbf{s}_0^\alpha = \mathbf{R}\mathbf{s}_{00}^\alpha, \quad \mathbf{l}_{00}^\alpha = \mathbf{s}_{00}^\alpha \times \mathbf{m}_{00}^\alpha \tag{B.10}$$

$$\mathbf{m}^\alpha = \mathbf{F}^{e^{-T}}\mathbf{m}_0^\alpha, \quad \mathbf{s}^\alpha = \mathbf{F}^e\mathbf{s}_0^\alpha, \quad \mathbf{l}^\alpha = \mathbf{s}^\alpha \times \mathbf{m}^\alpha \tag{B.11}$$

$$\mathbf{m}^\alpha = \mathbf{R}_t\mathbf{m}_{00}^\alpha, \quad \mathbf{s}^\alpha = \mathbf{R}_t\mathbf{s}_{00}^\alpha, \quad \mathbf{l}^\alpha = \mathbf{R}_t\mathbf{l}_{00}^\alpha \tag{B.12}$$